Master's Thesis

Hydrodynamic characteristics of swimming scallop, *Patinopecten yessoensis*

Jongwook Kim

Department of Mechanical Engineering

Graduate School of UNIST

2019

Hydrodynamic characteristics of swimming scallop, *Patinopecten yessoensis*

Jongwook Kim

Department of Mechanical Engineering

Graduate School of UNIST

Hydrodynamic characteristics of swimming scallop, *Patinopecten yessoensis*

A thesis
submitted to the Graduate School of UNIST
in partial fulfillment of the
requirements for the degree of
Master of Science

Jongwook Kim

07. 19. 2019
Approved by

Advisor
Jooha Kim

Hydrodynamic characteristics of swimming scallop, *Patinopecten yessoensis*

Jongwook Kim

This certifies that the thesis of Jongwook Kim is approved.

07/19/2019

signature

Advisor: Jooha Kim

signature

Jaeseon Lee: Thesis Committee Member #1

signature

Jae Hwa Lee: Thesis Committee Member #2

Abstract

Scallops are distinguished from other bivalves in that they can rapidly swim. One species of the scallop, *Patinopecten yessoensis* is known as inefficient swimmer or zigzag swimmer. Nevertheless *P. yessoensis* can swim long distance quickly. The scallop has reversed airfoil-like shape, and low aspect ratio (AR < 1.5). To investigated hydrodynamic characteristics of swimming scallop, swimming motion of the scallop is recorded, and the three-dimensional kinematics of swimming motion is analyzed. The scallop swims in the range of Reynolds number less than 45000. It also found that the scallop is not always jump but swims touching the ground. Directly forces and moment are measured by water tunnel experiment under 2 conditions, in ground effect and out of ground effect. Based on the results of forces and moment measurement, expected trajectory of swimming scallop is computed and compared with the trajectory of swimming actual scallop. By the comparison, quasi-steady state assumption of swimming scallop is verified so water tunnel experiment is validated. 2 step stall occurs out of ground effect. After first stall, lift is slightly decreased and increased again until second stall. As angle of attack increased, nonlinear lift is increased so lift coefficient reaches maximum right before second stall, because tip vortex helps the flow attach to the surface of the scallop. In case of typical 3-dimensional wing, lift is increased, and drag is decreased in ground effect, but in case of scallop, both lift and drag are increased. Multiple two-dimensional flow fields around the model out of ground effect are measured by conducting particle image velocimetry. During first stall, separation bubble from leading edge and wake region near the trailing edge encounter, so flow separation occurs over all surface of the model. However, tip-vortex induced downwash make the leading-edge vortex (LEV) attach to the surface, so lift is increased again. When angle of attack reaches 34°, tip-vortex induced downwash no longer formed over the scallop, and second stall occurs. Compared with that of level swimmer, hydrodynamic performance of zigzag swimmer is comparable to that of level swimmer. Therefore, zigzag swimmer is enough applicable to engineering problem.

Keywords: Zigzag swimmer, Ground effect, Low aspect ratio, Tip-vortex induced downwash

Contents

List of Figures

List of Tables

Nomenclature

Symbol

AR	Aspect ratio
$v_{xy,i}$	Velocity of scallop in xy plane of *i*th frame
$v_{x,i}$	x-velocity in *i*th frame
$v_{y,1,i}$	y-velocity in *i*th frame captured by camera 1
$Height_{meter}$	Metric height
$Height_{pixel,i}$	Pixel height in *i*th frame
$s_{x,i}$	x-coordinate of center of scallop in *i*th frame
$s_{y,1,i}$	y-coordinate of center of scallop in *i*th frame captured by camera1
t	Time
$v_{yz,i}$	Velocity of scallop in yz $v_{y,2,i}$ plane of *i*th frame
$v_{y,2,i}$	y-velocity in *i*th frame captured by camera 2
$v_{z,i}$	z-velocity in *i*th frame
$s_{y,2,i}$	y-coordinate of center of scallop in *i*th frame captured by camera2
v_i	Velocity of the scallop in *i*th frame
p	Commissure plane
$\vec{p}$	Normal vector of commissure plane
$\vec{c}$	Chord vector
$\vec{h}$	Hinge line vector
x_l	x-coordinate of leading edge
x_t	x-coordinate of trailing edge
y_l	y-coordinate of leading edge

y_t	y-coordinate of trailing edge
z_c	Unknown z-component of chord vector
x_h	Unknown x-component of hinge vector
$\vec{c}'$	Vector which is parallel to chord vector
$\vec{h}'$	Vector which is parallel to hinge vector
θ_{pitch}	Pitch angle
θ_{roll}	Roll angle
$\mathbf{h_{real,pixel}}$	Pixel hinge length of real scallop
$\mathbf{h_{real,meter}}$	Metric hinge length of real scallop
$\mathbf{h_{yz}}$	Hinge length projected to yz-plane
$\mathbf{\theta_{yaw}}$	Yaw angle
AoA	Angle of attack
$\mathbf{c}$	Chord
$\mathbf{s}$	Span
$\mathbf{A}$	Planform area
$\mathbf{Re}$	Reynolds number
$\mathbf{C_{M,c/4}}$	Moment coefficient at quarter chord
$\mathbf{C_{M,s}}$	Moment coefficient at strut
$\mathbf{x_s}$	Distance between strut and leading edge along x-axis
y_s	Distance between strut and leading edge along y-axis
$\mathbf{C_L}$	Lift coefficient
$\mathbf{C_D}$	Drag coefficient
N	Normal force from ground

r	Distance from center of mass to trailing edge of scallop
θ	Pitch angle
ρ	Density of scallop
ρ_w	Density of water
m	mass of the scallop
β	Angle between the velocity ($\vec{V}$) and the ground
g	Gravitational constant
$\forall$	Volume of the scallop
f	Friction coefficient
I_m	Pitching moment of inertia
$C_{M,CoM}$	Moment coefficient at center of mass
α	Angle of attack
$y_{i,volume}$	Vertical distance between center of mass of scallop and the lowest point of scallop
FoV	Field of view
u_{rms}	Root-mean square of streamwise velocity
U	Freestream velocity
$C_{L,max}$	Maximum value of C_L
$AoA_{CL,max}$	Angle of attack, when C_L has the maximum value
h_{CL}	Distance between center of pressure and the leading edge
ω	Vorticity
x_{sep}	Locations of separation point
LEV	Leading edge vortex
L	Lift

D	Drag

1. Introduction

Most bivalves do not move their habitation but live in a place where they settled (Bayne and Newell 1983). By these habits, bivalves are prone to be eaten by predators. Thus, most bivalves bury themselves in the ground to avoid predators, and some, such as mussels, stick their bodies on hard surfaces. Most of these sedentary bivalves have solid shells to protect themselves from predators. Starfish, however, break the protection strategy of bivalve by opening the shells with tentacles and eating them by putting the stomach into it (Feder 1955).

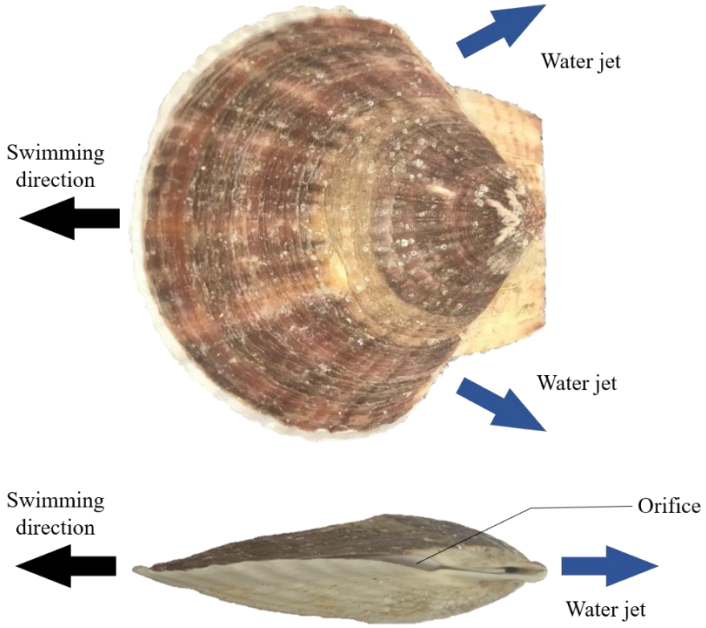

Figure 1. Directions of swimming and water jet during scallop swimming.

Distinguished from other bivalves, scallops have unique ability to swim for keeping their bodies from predators (Gosling 2008). When a scallop encounters a predator such as a starfish, as shown in figure 1, it can swim in ventral direction perpendicular to the hinge line by quickly closing the two shells and expelling water into the orifice on either side of the hinge (Moore and Trueman 1971). Scallops can use these swimming skills to move their habitation or to successfully escape from predators.

The shell morphology and the swimming behaviour varies depending on the scallop genera (Stanley 1970). Based on the shell shape and the swimming locomotion, scallops can be divided into 2 groups, level swimmers and zigzag swimmers (Hayami 1991). Level swimmers include *Placopecten* and *Amusium*. The shell of level swimmers is thin and weakly upward-convex, so they

have airfoil like shape. Level swimmers have shallow surface grooves on the shells. According to Caddy (1968), one of level swimmer, *Placopecten magellanicus*, jump from 30° to 50° to swim. Then it moves up to 4m while maintaining altitude. This is called level flight. There are several factors that make the scallops to swim distance of several times of their body length without sinking. According to Vogel (1997), the muscles of the *Placopecten magellanicus* are tuned appropriately for swimming. Anderson *et al*. (1997) suggested the possibility that the surface grooves on shells of *Placopecten magellanicus* can reduce drag while swimming. Studies also carried out to measure hydrodynamic property of level swimmers using towing tank or water tunnel (Gruffydd 1976; Hayami 1991; Milward and Whyte 1992).

Zigzag swimmers include *Patinopecten*, *Argopecten*. The shell of zigzag swimmers is thick and equiconvex or strongly downward convex, resulting flow separation on the surface when swimming so they are known to swim awkward to zigzag. They have relatively large surface grooves on the shell. Choi *et al*. (2012) showed that surface grooves on the shell of *Patinopecten yessoensis* increases hydrodynamic performance of the scallop through wind tunnel experiments. Milward and Whyte (1992), on the other hand, found that surface grooves on the shell of *Pecten alba* do not significantly affect hydrodynamic performance using water tunnel.

Above studies measuring the hydrodynamic performance of surface grooves of zigzag swimmers have two limitations, so the result is different to each other. First limitation is that swimming motion of scallop is assumed to be a steady motion. However, while actual scallop is swimming, instantaneous velocity and pitch angle are constantly changing and shape of the scallop is also not consistent because of successive adduction, so swimming motion of the scallop is not steady motion. Considering these factors, quasi-steady assumption of swimming scallop is needed to be verified. The second limitation is that the scallops do not always jump high, but they swim on the ground when they move a short distance so hydrodynamic performance in ground effect also needs to be studied.

The surface grooves on zigzag swimmers are much larger (by about 7-8 times) than those on level swimmers (Anderson *et al*. 1997, Choi *et al*. 2012). It should be noted here that for a surface device, too small a size may hamper its applicability to engineering problems due to operational factors such as dust accumulation (Sagong *et al*. 2008). Therefore, if any improvement in hydrodynamic (or aerodynamic) performance is possible, large surface grooves of zigzag swimmers have a high potential to be implemented in practical applications such as low-aspect-ratio wings used in small UAVs (unmanned aerial vehicles). In this context, it is important to analyze the hydrodynamic function of large surface grooves of zigzag swimmers in scallop swimming.

Before researching hydrodynamic performances of surface grooves on the shell of zigzag swimmers, the hydrodynamic characteristics of zigzag swimmers must be analyzed. There are 4 main hydrodynamic characteristics of swimming zigzag swimmers. First characteristics is cross section shape. The cross section of the zigzag swimmer is similar to a reversed airfoil having sharp leading edge and blunt trailing edge. Lind *et al*. (2014) studied a two-dimensional reversed airfoil (NACA0012) which is thinner than the scallop. At angle of attack is 0°, wake region is formed behind the airfoil, and at angle of attack is 6°, leading edge stall occurs. Second one is planform shape of the scallop. Zigzag swimmers have circular planform shape and have low aspect ratio. Third one is Reynolds number of the scallop. Zigzag swimmers are small, so they swim in the range of low Reynolds number. Torres and Mueller (2004) reported that elliptical planform wing which has low aspect ratio (AR < 2) is stalled at higher angle of attack than high aspect ratio wing because of tip vortex. The last characteristics of the scallop is ground effect. Since the scallop swims on the ground, flow around the scallop is affected by ground. Traub (2014) investigated low aspect ratio wing (AR < 5) in ground effect experimentally and analytically and found that lift is increased and drag is decreased in ground effect. Since the zigzag swimmer has above 4 characteristics, it is necessary to study the hydrodynamic characteristics.

Therefore, the objective of this thesis is to investigate the hydrodynamic characteristics of zigzag-swimmer scallop, *Patinopecten yessoensis*. For this purpose, the kinematics of the actual scallop *Patinopecten yessoensis* was measured and based on the measured kinematics, the water tunnel experiment was conducted. Hydrodynamic forces and moments were measured under 2 conditions, in ground effect and out of ground effect using water tunnel. Quasi steady state of swimming scallop was verified through the measured forces and moment. Finally, the flow around scallops was quantitatively analyzed by digital particle image velocimetry (DPIV).

2. Experimental setup

2.1. Measurement of kinematic data of actual scallop

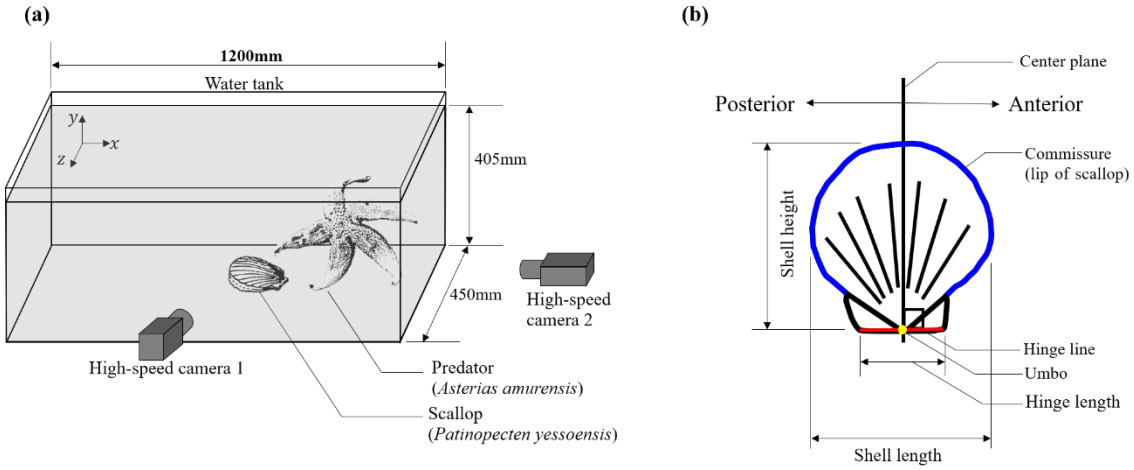

Figure 2. (a) Schematic diagram of the experimental setup for measurement of kinematic data and (b) left (upper) valve of scallop.

Sample name	Shell length (mm)	Shell height (mm)	Hinge length (mm)	Mass (g)	Number of movements
A	84	82.7	39.5	71.4	11
B	69.55	60.8	29.6	58	1
C	83.45	84.15	33.55	62.1	7
D	73.2	73	26.85	54.9	6
E	87.8	85.9	38.7	106.2	4
F	80	79.5	31	65	7
G	75.2	68.6	28.8	65.2	2
H	75.5	77.25	33	74.1	3
I	75.3	74.25	30.5	58.9	2

Table 1 Specification of specimens for measurement of kinematic data

To know the kinematics of swimming scallop, *Patinopecten yessoensis,* 43 movements of 9 scallops were recorded. *Patinopecten yessoensis* was provided by the East Sea Fisheries Research Institute of the National Institute of Fisheries Science, Gangneung. At the nearby harbor, starfishes, *Asterias amurensis*, which are predator of *Patinopecten yessoensis* according to Dautov & Karpenko (1984), are captured to stimulate the scallop to swim. Figure 2(a) shows experimental setup used to

measure kinematic data of swimming scallop. To measure 3-dimensional motion of the scallops, 2 high speed cameras with resolution of 1280 × 800 pixels (Dantec Dynamics Speedsense) are used. Camera 1 and 2 recorded xy-plane and yz-plane (figure 3(a) and (b)) respectively. The movies have a time resolution of 50 frames per second. The water tank used in the experiment is made of glass, 1200mm long, 450mm wide and was filled with 16°C seawater at a depth of 405mm. the water tank is large enough not to affect swimming of the scallop.

Figure 2(b) shows schematic diagram of left (upper) valve of a scallop. A line which is along hinge of the scallop, is called hinge line (red line in figure 2(b)). On the hinge, a protruding part near the center of the hinge is called umbo (yellow point in figure 2(b)), on which trailing edge is. The point on the shell edge which is the furthest from umbo is called leading edge, and the line connecting umbo and leading edge is defined as chord (white line at figure 3(a)) and the distance of chord is called chordlength or height. The greatest distance between 2 points on the shell edge, along the line parallel to hinge line is called length (white line at figure 3(b)). Length also called as span because the line connecting the 2 points are almost perpendicular to chord (Martin *et al*. 2000). Angle of attack is defined as the angle between velocity of the scallop and the plane on which lip of the scallop lies (Dadswell and Weih, 1990). Lip of the scallop is defined as the line where the upper shell and the lower shell meet (blue line in figure 1(b)), and it also called as commissure.

The specification of the specimens is in table 1. Averaged mass of the specimens is 68.7g, averaged height is 76.2mm and averaged length is 78.2mm. Hinge length means the length of the hinge line (red line in figure 1(b)). Before measuring mass of samples, all samples were taken out from the water tank and the water in the shell was removed. According to Silina (2008), *P. yessoensis* which is healthy young jumps to distances as long as 100 cm, but the adult scallop jumps only 40cm. In addition, a scallop, *P. magellanicus,* of which length is larger than 70mm and smaller than 100mm can keep pace without falling or captured by predators (Caddy 1968), so almost specimens have length which is within the range.

Velocity of the scallop is defined as velocity of the center of the scallop. Figure 3(a) and (b) shows how center of the scallop is defined. Center of the scallop (blue point) is located at midpoint of the chordline in xy-plane (figure 3(a)), and midpoint of the line connecting the rightmost point and leftmost point of the scallop shell (red point) in yz-plane (figure 3(b)). Velocities of the scallop at i^{th} frame in xy- and yz-plane (denoted by $v_{xy,i}$ and $v_{yz,i}$ respectively) are calculated as follows.

$$\boldsymbol{v_{xy,i}} = \left(\boldsymbol{v_{x,i}}, \boldsymbol{v_{y,1,i}}\right) = \left(\frac{s_{x,i+1}-s_{x,i-1}}{2\Delta t}, \frac{s_{y,1,i+1}-s_{y,1,i-1}}{2\Delta t}\right) \times \frac{\boldsymbol{Height_{meter}}}{\boldsymbol{Height_{pixel,i}}} \quad (1)$$

$$\boldsymbol{v_{yz,i}} = \left(\boldsymbol{v_{y,2,i}}, \boldsymbol{v_{z,i}}\right) = \left(\frac{s_{y,2,i+1}-s_{y,2,i-1}}{2\Delta t}, \frac{s_{z,i+1}-s_{z,i-1}}{2\Delta t}\right) \times \frac{\boldsymbol{Length_{meter}}}{\boldsymbol{Length_{pixel,i}}} \quad (2)$$

where subscript pixel and denotes the unit of the value. $Height_{pixel,i}$ and $Length_{pixel,i}$ are shown in figure 3, and $Height_{meter}$ and $Length_{meter}$ are shown in table 1. The ratio of height in meter and pixel is multiplied to unit conversion as shown in equation (1). Since the scallop rotated about the z-axis, the distances from rightmost point to leftmost point (shown in figure 3(b)) is not actual length. However, the distance is almost the same with length because planform shape of the scallop is almost circular, so ratio of the lengths also multiplied as shown in equation (2). Velocity in y-direction can be calculated in both xy- and yz-plane, so the average value is used. Finally, 3-dimensional velocity of the scallop is calculated as

$$\boldsymbol{v_i} = \left(\boldsymbol{v_{x,i}},\ \frac{1}{2}\left(\boldsymbol{v_{y,1,i}} + \boldsymbol{v_{y,2,i}}\right),\ \boldsymbol{v_{z,i}}\right) \quad (3)$$

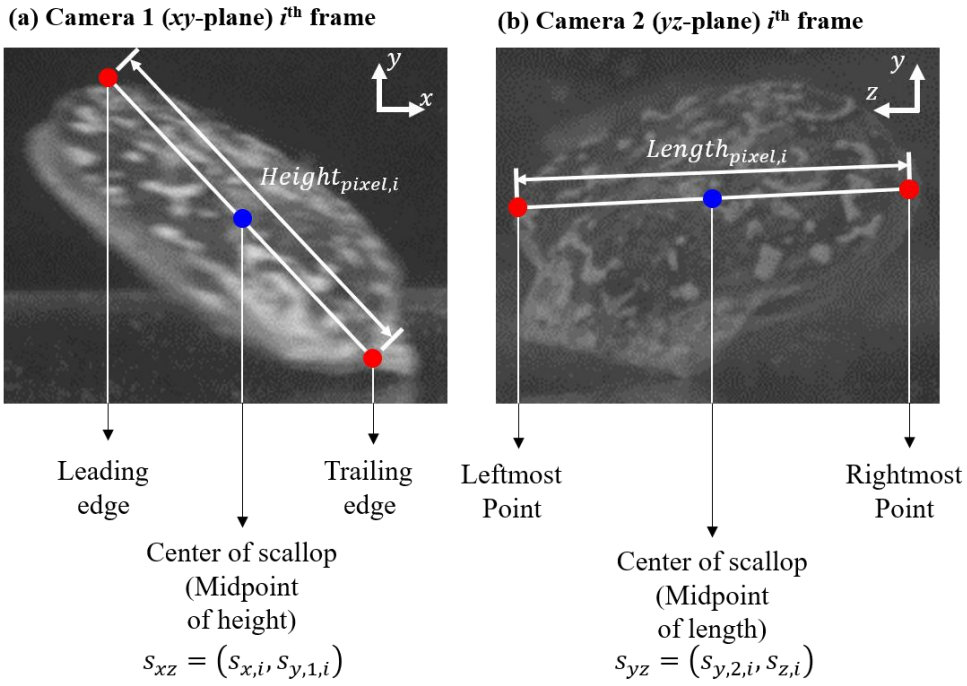

Figure 3. Image analysis for calculating velocity of scallop swimming (a) xy-plane which is captured by camera1; (b) yz-plane which is captured by camera2.

To calculate angle of attack at each frame, the commissure plane p is suggested, on which lip of the scallop lies. The commissure plane p has normal vector of $\vec{p}$ which has the following characteristics.

$$\vec{p} \perp \vec{c}, \quad (4)$$

$$\vec{p} \perp \vec{h} \quad (5)$$

$\vec{h}$ and $\vec{c}$ denotes vectors which is on the hinge line, and chordline respectively (white arrow in figure 4(a) and 4(b)). $\vec{c}$ and $\vec{h}$ are calculated as

$$\vec{c} = (x_l - x_t,\ y_l - y_t,\ z_c), \tag{6}$$

$$\vec{h} = (x_h,\ y_p - y_a,\ z_p - z_a) \tag{7}$$

$(x_l,\ y_l)$ and $(x_t,\ y_t)$ are position coordinates of leading edge and trailing edge in figure 4(a), respectively. $(y_a,\ z_a)$ and $(y_p,\ z_p)$ are position coordinates of the most anterior and most posterior point on hinge of the scallop in figure 4(b), respectively. y_c in equation (6) and x_h in equation (7) are unknown component of vector $\vec{c}$ and $\vec{h}$ because they are normal component to xy-plane (figure 4(a)), and yz-plane (figure 4(b)), respectively. Since we need information about only direction, each component in the vectors can be divided as the same factors. Thus, rewriting equation (6) and (7) as

$$\vec{c}' = \frac{\vec{c}}{x_l - x_t} = \left(1,\ \frac{y_l - y_t}{x_l - x_t},\ \frac{z_c}{x_l - x_t}\right), \tag{8-1}$$

$$\vec{h}' = \frac{\vec{h}}{z_p - z_a} = \left(\frac{x_h}{z_p - z_a},\ \frac{y_p - y_a}{z_p - z_a},\ 1\right) \tag{9-1}$$

In equation (8-1) and (9-1), y-components can be substituted as tangent function (in figure 4(a), and 4(b)) and fraction components can be written simpler as $z_c/(x_l - x_t) = z_c'$ and $x_h/(z_p - z_a) = x_h'$. Then, the vectors are as follows

$$\vec{c}' = (1,\ \tan\theta_{pitch},\ z_c'), \tag{8-2}$$

$$\vec{h}' = (x_h',\ \tan\theta_{roll},\ 1) \tag{9-2}$$

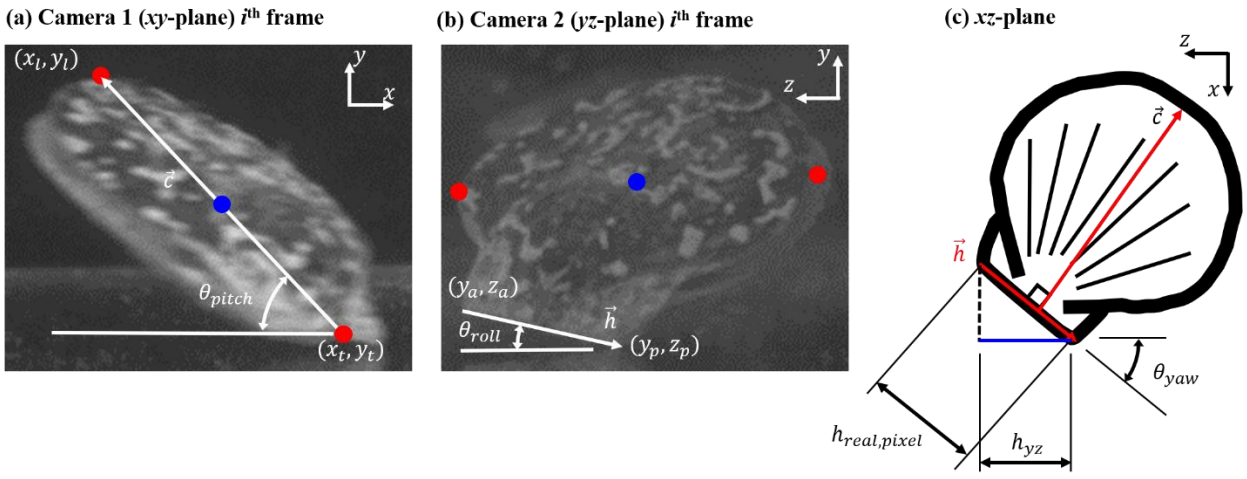

Figure 4. Image analysis for calculating angle of attack of scallop swimming (a) xy-plane which is captured by camera1; (b) yz-plane which is captured by camera2; (c) xz-plane.

Suppose hinge length of the scallop in pixel ($h_{real,pixel}$), which is calculated by

$$\mathbf{h_{real,pixel}} = \mathbf{h_{real,meter}} \times \frac{\mathbf{length_{pixel}}}{\mathbf{length_{meter}}} \quad (10)$$

where $h_{real,meter}$ is metric hinge length in Table 1 and the unit is converted as velocity calculation. Then, projected hinge length on yz-plane (h_{yz}) is used to find the exact value of θ_{yaw}. θ_{yaw} can be calculated by following equation.

$$\cos\theta_{yaw} = \frac{h_{yz}}{h_{real,pixel}} = \frac{\sqrt{(y_p - y_a)^2 + (z_p - z_a)^2}}{h_{real,pixel}} \quad (11)$$

Combining equation (9-2) and (11), x_h' can be calculated as following equations.

$$\cos\theta_{yaw} = \frac{\sqrt{1+\tan^2\theta_{roll}}}{|\vec{h}'|} = \sqrt{\frac{\tan^2\theta_{roll}+1}{x_h'^2+\tan^2\theta_{roll}+1}} \quad (12)$$

Now, all 3 components of $\vec{h}$ is known, and it is as follows.

$$\vec{h}' = \left(tan\theta_{yaw}\sqrt{1+\tan^2\theta_{roll}},\ \tan\theta_{roll},\ \ 1\right) \quad (13)$$

Then, $\vec{c}$ can be calculated, because $\vec{c}$ is perpendicular to $\vec{h}$, and $\vec{h} \cdot \vec{c} = 0$. $\vec{c}$ is known as follows.

$$\vec{c}' = \left(1,\ \tan\theta_{pitch},\ -\tan\theta_{yaw}\sqrt{1+\tan^2\theta_{roll}} - \tan\theta_{roll}\tan\theta_{pitch}\right) \quad (14)$$

Exact direction of $\vec{p}$ can be calculated by $\vec{h}' \times \vec{c}'$ which is derived from equation (1) and (2).

$$\vec{p} = \begin{vmatrix} \hat{i} & \hat{j} & \hat{k} \\ \tan\theta_{yaw}\sqrt{1+\tan^2\theta_{roll}} & \tan\theta_{roll} & 1 \\ 1 & \tan\theta_{pitch} & -\tan\theta_{yaw}\sqrt{1+\tan^2\theta_{roll}} - \tan\theta_{roll}\tan\theta_{pitch} \end{vmatrix} \quad (15)$$

Finally angle of attack is found using following equation, because it is defined as the angle between the velocity of the scallop swimming ($\vec{V}$) and the planform.

$$AoA = sin^{-1}\frac{\vec{V}\cdot\vec{p}}{|\vec{V}||\vec{p}|} \quad (16)$$

2.2. Forces and moment measurement

To measure the hydrodynamic forces and moments acting on the scallops, we conducted water tunnel experiment. Lift, drag and pitching moment were measured. The force measurements were

conducted for two cases: when the scallop swims in ground effect and out of ground effect. The scallop model was made of enlarging the size of the *Patinopecten yessoensis* shell A (Table 1) by 2 times larger than the actual size, because scallop A moved the most times. Actual scallop is 3D scanned using 3D scanning system (DAVID SLS-3-3D) in resolution of 0.05mm, and a model is made by nylon at UDMC in UNIST using 3D printer (EOS P770) which resolution is 0.1mm. The model has height of 165.4mm and length of 169mm. Height and length are used as chord (c) and span (s), respectively. Planform area (A) of the scallop is 21088mm^2, so aspect ratio (s^2/A) is 1.35. The thickness of the model is 46mm (0.28c). The model when viewed on the posterior side is very similar to reversed symmetric airfoil (figure 5) which has sharp leading edge and blunt trailing edge. Based on the kinematics of the actual scallop swimming, the experiment is conducted in the range of Reynolds number (based on the height of the scallop) Re = 20000 - 45000. The schematic diagram of experimental setup is shown in figure 6. Angle of attack varied from 0° to 50° by 2°. The streamwise length, width and depth of the water tunnel test section are respectively 1200mm×500mm×460mm. Freestream turbulence of test section is less than 3% at every Re. Strut was attached to the most posterior point of the scallop (figure 5) in the length-direction to prevent flow interpretation. The strut was designed to be very thin with a diameter of 3mm to minimize the effect of strut. In the experiment, two loadcells (CAS BCA-5L) for lift and drag and a torque sensor (QMSYSTEM QMF-1) for pitching moment were installed at the other side of the strut. The moment coefficient at quarter chord ($C_{M,c/4}$) is calculated by

$$C_{M,c/4} = C_{M,s} - \left\{\left(\frac{x_s}{c} - \frac{1}{4}\right)\cos\alpha + \frac{y_s}{c}\sin\alpha\right\} C_L - \left\{\left(\frac{x}{c} - \frac{1}{4}\right)\sin\alpha - \frac{y_s}{c}\cos\alpha\right\} C_D \quad (17)$$

where $C_{M,s}$ is moment coefficient at position of strut, x_s and y_s is distances from leading edge in direction of x- and y-axis in figure 5, respectively.

Ground is made by acryl plate of which length in streamwise direction is 500mm (3.03c), and it is installed next to the right (lower) valve of the model. When angle of attack is 0°, leading edge of model is 100mm away from leading edge of ground in streamwise direction. Considering kinematics of the scallop (See sec. 3.1), scallops always swim touching the ground. However, since the force and moment cannot be measured when the ground is touched, the ground and the model are kept at a minimum distance of 1 mm (0.006c). As the angle of attack increases, the plate is moved in the y direction so that the distance between the scallop and the plate does not change. For each AoA, a camera (Dantec Dynamics Speedsense) was installed at the bottom of the scallop to measure the distance between the scallop and the plate. The spatial resolution of the camera used for distance measurement is 0.15 mm/px.

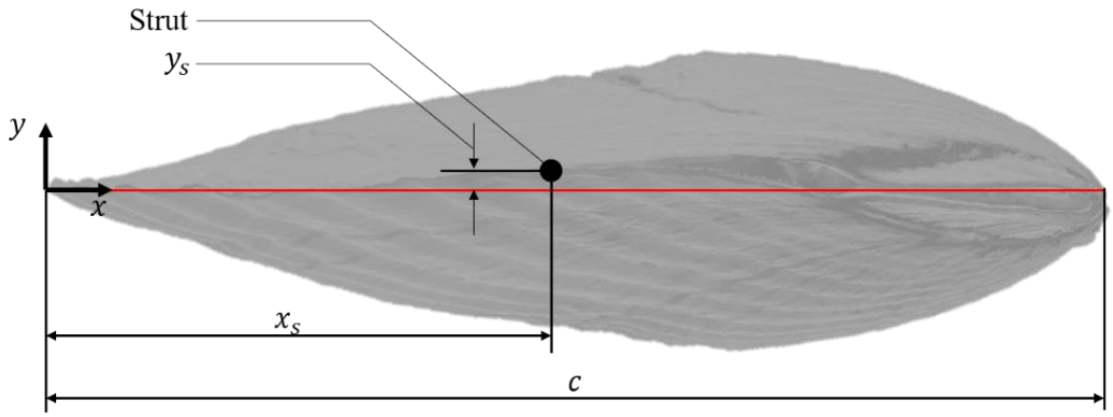

Figure 5. Posterior view of the model.

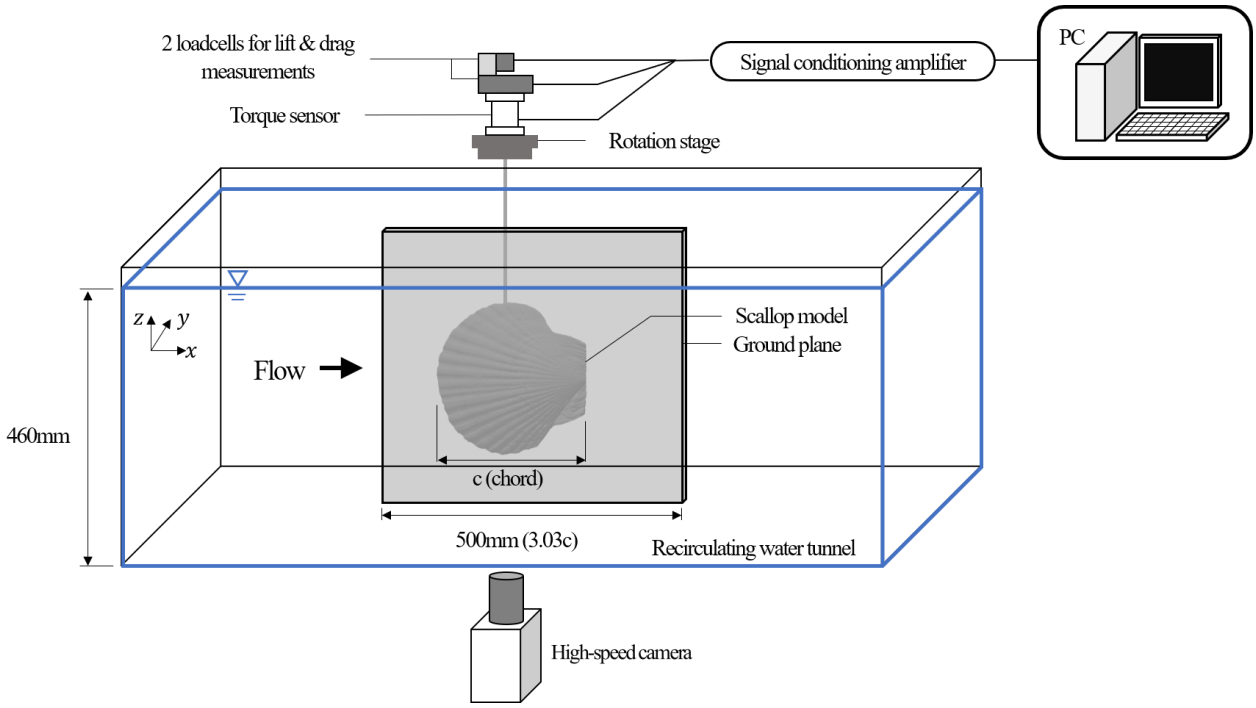

Figure 6. Schematic diagram of the experimental setup for force and moment measurement.

2.3. Trajectory of swimming scallop simulation

Prior to analyzing the hydrodynamic characteristics of the scallop, it is necessary to guarantee that the flow around the model in water tunnel experiment satisfies hydrodynamic similarity with the flow around the swimming actual scallop. The trajectory of the scallop was computed using the forces and moment obtained from the experiment in ground effect, and the computed trajectory was compared

with the trajectory of swimming actual scallop. Since the forces and moment are measured in steady state, computed trajectory is steady state, while trajectory of actual scallop is not steady state. If the two trajectories are similar, actual scallop swimming can be assumed to be quasi-steady state and water tunnel experiment will satisfy the hydrodynamic similarity with the flow around the actual scallop.

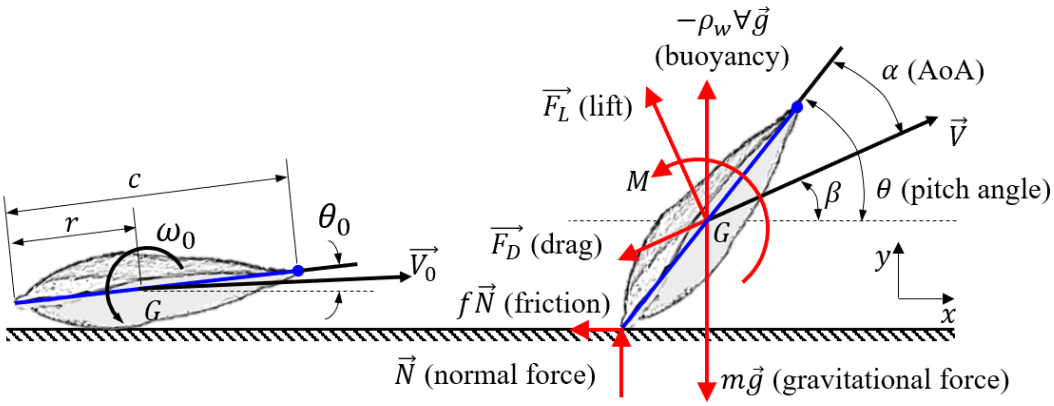

Figure 7. Free body diagram for trajectory computation.

Trajectory is computed under two assumptions for convenience. The first assumption is that the movement of scallop is two-dimensional. The second assumption is that the shape of the scallop is a zero-volume rod. However, when computing angle of attack, the second assumption was not applied for accurate calculation, but the actual volume of scallops was considered. A detailed explanation follows later. Figure 7 shows all the forces and moments applied to the scallop while swimming, and the equations of motions are

$$N = \frac{r\ddot{\theta}cos\theta - \left\{\frac{\rho|\vec{V}|^2 A}{2m}(C_L cos\beta - C_D sin\beta) - g + \frac{\rho_w g \forall}{m}\right\} - r\dot{\theta}^2 sin\theta}{\frac{r^2 cos\theta(cos\theta + fsin\theta)}{I_m} + \frac{1}{m}}, \quad (18)$$

$$\ddot{\theta} = f_\theta(|\vec{V}|, \theta, \alpha) = \frac{\rho|\vec{V}|^2 Ac}{2I_m} C_{M,CoM} - \frac{Nr(cos\theta + fsin\theta)}{I_m}, \quad (19)$$

$$\ddot{x} = f_x(|\vec{V}|, \theta, \alpha) = -\frac{\rho|\vec{V}|^2 A}{2m}(C_D cos\beta + C_L sin\beta) - \frac{fN}{m}, \quad (20)$$

$$\ddot{y} = f_y(|\vec{V}|, \theta, \alpha) = \frac{\rho|\vec{V}|^2 A}{2m}(C_L cos\beta - C_D sin\beta) - g + \frac{\rho_w g \forall}{m} + \frac{N}{m} \quad (21)$$

where N is normal force from ground, r is the distance from center of mass to trailing edge of

scallop and θ is pitch angle. ρ and ρ_w are density of scallop and water respectively, m is mass of the scallop and A is planform area of scallop shell. β is the angle between the velocity ($\vec{V}$) and the ground, g is gravitational constant and ∀ is volume of the scallop. f is friction coefficient between wet glass bottom and scallop shell and I_m is pitching moment of inertia at center of mass. x and y are center of mass position of the scallop in horizontal and vertical direction respectively. Lift (C_L), drag (C_D) and moment coefficient ($C_{M,CoM}$) are all functions of Re, and AoA (α), that is functions of $\vec{V}$ and α. $C_{M,CoM}$ is moment coefficient at center of mass, and it is calculated using moment at the most posterior point at which strut is attached. Friction coefficient between wet glass bottom and scallop shell is measured by multi-function adhesion scratch test system (Neoplus AST210). I_m was measured with 3D-scanned model data (See secion 2.2) on the assumption of constant density.

In the integration for the trajectory calculation, 4th-order Runge-Kutta method with a time interval (Δt) of 0.0002 seconds between steps is used and the calculation formula of each step is as follows.

$$\left|\vec{V}\right|_{i,1} = \left|\vec{V}\right|_i, \quad (22)$$

$$\theta_{i,1} = \theta_i, \quad (23)$$

$$\alpha_{i,1} = \alpha_i, \quad (24)$$

$$\dot{x}_{i,1} = \left|\vec{V}\right|_i cos\theta_i, \quad (25)$$

$$\dot{y}_{i,1} = \left|\vec{V}\right|_i sin\theta_i, \quad (26)$$

$$\dot{\theta}_{i,1} = \dot{\theta}_i, \quad (27)$$

$$\ddot{x}_{i,1} = f_x\left(\left|\vec{V}\right|_{i,1}, \theta_{i,1}, \alpha_{i,1}\right), \quad (28)$$

$$\ddot{y}_{i,1} = f_y\left(\left|\vec{V}\right|_{i,1}, \theta_{i,1}, \alpha_{i,1}\right), \quad (29)$$

$$\ddot{\theta}_{i,1} = f_\theta\left(\left|\vec{V}\right|_{i,1}, \theta_{i,1}, \alpha_{i,1}\right), \quad (30)$$

$$\dot{x}_{i,2} = \dot{x}_{i,1} + \ddot{x}_{i,1}\left(\frac{1}{2}\Delta t\right), \quad (31)$$

$$\dot{y}_{i,2} = \dot{y}_{i,1} + \ddot{y}_{i,1}\left(\frac{1}{2}\Delta t\right), \quad (32)$$

$$\dot{\theta}_{i,2} = \dot{\theta}_{i,1} + \ddot{\theta}_{i,1}\left(\frac{1}{2}\Delta t\right), \quad (33)$$

$$\theta_{i,2} = \theta_{i,1} + \dot{\theta}_{i,1}\left(\frac{1}{2}\Delta t\right), \quad (34)$$

$$\boldsymbol{\alpha_{i,2} = \theta_{i,2} - tan^{-1}\frac{\dot{y}_{i,2}+\dot{y}_{i,2,volume}}{\dot{x}_{i,2}}},\quad (35)$$

$$\boldsymbol{\ddot{x}_{i,2} = f_x(\dot{x}_{i,2}, \dot{y}_{i,2}, \alpha_{i,2})},\quad (36)$$

$$\boldsymbol{\ddot{y}_{i,2} = f_y(\dot{x}_{i,2}, \dot{y}_{i,2}, \alpha_{i,2})},\quad (37)$$

$$\boldsymbol{\ddot{\theta}_{i,2} = f_\theta(\dot{x}_{i,2}, \dot{y}_{i,2}, \alpha_{i,2})},\quad (38)$$

$$\boldsymbol{\dot{x}_{i,3} = \dot{x}_{i,1} + \ddot{x}_{i,2}\left(\frac{1}{2}\Delta t\right)},\quad (39)$$

$$\boldsymbol{\dot{y}_{i,3} = \dot{y}_{i,1} + \ddot{y}_{i,2}\left(\frac{1}{2}\Delta t\right)},\quad (40)$$

$$\boldsymbol{\dot{\theta}_{i,3} = \dot{\theta}_{i,1} + \ddot{\theta}_{i,2}\left(\frac{1}{2}\Delta t\right)},\quad (41)$$

$$\boldsymbol{\theta_{i,3} = \theta_{i,1} + \dot{\theta}_{i,2}\left(\frac{1}{2}\Delta t\right)},\quad (42)$$

$$\boldsymbol{\alpha_{i,3} = \theta_{i,3} - tan^{-1}\frac{\dot{y}_{i,3}+\dot{y}_{i,3,volume}}{\dot{x}_{i,3}}},\quad (43)$$

$$\boldsymbol{\ddot{x}_{i,3} = f_x(\dot{x}_{i,3}, \dot{y}_{i,3}, \alpha_{i,3})},\quad (44)$$

$$\boldsymbol{\ddot{y}_{i,3} = f_y(\dot{x}_{i,3}, \dot{y}_{i,3}, \alpha_{i,3})},\quad (45)$$

$$\boldsymbol{\ddot{\theta}_{i,3} = f_\theta(\dot{x}_{i,3}, \dot{y}_{i,3}, \alpha_{i,3})},\quad (46)$$

$$\boldsymbol{\dot{x}_{i,4} = \dot{x}_{i,1} + \ddot{x}_{i,3}\Delta t},\quad (47)$$

$$\boldsymbol{\dot{y}_{i,4} = \dot{y}_{i,1} + \ddot{y}_{i,3}\Delta t},\quad (48)$$

$$\boldsymbol{\dot{\theta}_{i,4} = \dot{\theta}_{i,1} + \ddot{\theta}_{i,3}\Delta t},\quad (49)$$

$$\boldsymbol{\theta_{i,4} = \theta_{i,1} + \dot{\theta}_{i,3}\Delta t},\quad (50)$$

$$\boldsymbol{\alpha_{4,i} = \theta_{i,4} - tan^{-1}\frac{\dot{y}_{i,4}+\dot{y}_{i,4,volume}}{\dot{x}_{i,4}}},\quad (51)$$

$$\boldsymbol{\ddot{x}_{i,4} = f_x(\dot{x}_{i,4}, \dot{y}_{i,4}, \alpha_{i,4})},\quad (52)$$

$$\boldsymbol{\ddot{y}_{i,4} = f_y(\dot{x}_{i,4}, \dot{y}_{i,4}, \alpha_{i,4})},\quad (53)$$

$$\boldsymbol{\ddot{\theta}_{i,4} = f_\theta(\dot{x}_{i,4}, \dot{y}_{i,4}, \alpha_{i,4})},\quad (54)$$

$$\boldsymbol{x_{i+1} = x_{i,1} + \frac{\Delta t}{6}(\dot{x}_{i,1} + 2\dot{x}_{i,2} + 2\dot{x}_{i,3} + \dot{x}_{i,4})},\quad (55)$$

$$\boldsymbol{y_{i+1} = y_{i,1} + \frac{\Delta t}{6}(\dot{y}_{i,1} + 2\dot{y}_{i,2} + 2\dot{y}_{i,3} + \dot{y}_{i,4})},\quad (56)$$

$$\boldsymbol{\theta_{i+1} = \theta_{i,1} + \frac{\Delta t}{6}(\dot{\theta}_{i,1} + 2\dot{\theta}_{i,2} + 2\dot{\theta}_{i,3} + \dot{\theta}_{i,4})},\quad (57)$$

$$\dot{\boldsymbol{x}}_{\boldsymbol{i+1}} = \dot{\boldsymbol{x}}_{\boldsymbol{i,1}} + \frac{\Delta \boldsymbol{t}}{\boldsymbol{6}}\left(\ddot{\boldsymbol{x}}_{\boldsymbol{i,1}} + \boldsymbol{2}\ddot{\boldsymbol{x}}_{\boldsymbol{i,2}} + \boldsymbol{2}\ddot{\boldsymbol{x}}_{\boldsymbol{i,3}} + \ddot{\boldsymbol{x}}_{\boldsymbol{i,4}}\right), \quad (58)$$

$$\dot{\boldsymbol{y}}_{\boldsymbol{i+1}} = \dot{\boldsymbol{y}}_{\boldsymbol{i,1}} + \frac{\Delta \boldsymbol{t}}{\boldsymbol{6}}\left(\ddot{\boldsymbol{y}}_{\boldsymbol{i,1}} + \boldsymbol{2}\ddot{\boldsymbol{y}}_{\boldsymbol{i,2}} + \boldsymbol{2}\ddot{\boldsymbol{y}}_{\boldsymbol{i,3}} + \ddot{\boldsymbol{y}}_{\boldsymbol{i,4}}\right), \quad (59)$$

$$\dot{\boldsymbol{\theta}}_{\boldsymbol{i+1}} = \dot{\boldsymbol{\theta}}_{\boldsymbol{i,1}} + \frac{\Delta \boldsymbol{t}}{\boldsymbol{6}}\left(\ddot{\boldsymbol{\theta}}_{\boldsymbol{i,1}} + \boldsymbol{2}\ddot{\boldsymbol{\theta}}_{\boldsymbol{i,2}} + \boldsymbol{2}\ddot{\boldsymbol{\theta}}_{\boldsymbol{i,3}} + \ddot{\boldsymbol{\theta}}_{\boldsymbol{i,4}}\right), \quad (60)$$

$$\boldsymbol{\alpha}_{\boldsymbol{i+1}} = \boldsymbol{\theta}_{\boldsymbol{i+1}} - \tan^{-1}\frac{\dot{\boldsymbol{y}}_{\boldsymbol{i+1}} + \dot{\boldsymbol{y}}_{\boldsymbol{i+1,volume}}}{\dot{\boldsymbol{x}}_{\boldsymbol{i+1}}} \quad (61)$$

Since the scallop is assumed to be a zero-volume rod, trailing edge of the scallop is always attached to ground, but during the real scallop swimming, the point on the scallop, which is attached to ground keeps changing, because of round bottom shape of the scallop. It causes little error of dislocation in y-direction. For calculating velocity, this change is negligibly small, but for calculating angle of attack, the error must be corrected. Hence, $\dot{y}_{i+1,volume}$ and $\dot{y}_{i,n,volume}$ $(n = 2,3,4)$ are considered in each step of calculating angle of attack. $\dot{y}_{i+1,volume}$ and $\dot{y}_{i,n,volume}$ $(n = 2,3,4)$ means how much the distance between center of mass of scallop and the lowest point of scallop ($y_{i,volume}$ in figure 8) is changed as pitch angle of scallop being changed from $\theta_{i,1}$ to θ_{i+1} or $\theta_{i,n}$ $(n = 2,3,4)$.

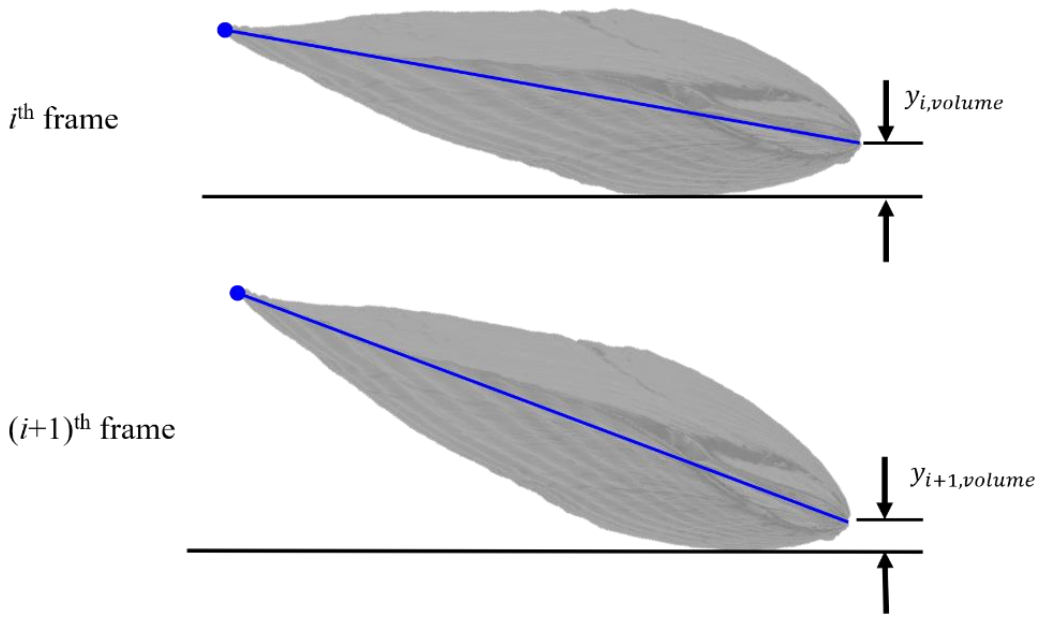

Figure 8. The distance between center of mass of scallop and the lowest point of scallop.

2.4. Particle image velocimetry

The experimental setup for particle image velocimetry (PIV) to measure flow field around the model is shown schematically in figure 9. The PIV measurement was performed in the same water tunnel used for the force measurement. The PIV system consist of a high-speed camera which is used to measure kinematics of swimming scallop (see section 2.1.) a continuous DPSS laser of 5W output power (MGL-N-532) and laser mirror to prevent shadows of the model. Hollow glass, of which diameter is approximately 10μm, is used as tracing particle. Since the model has 3-dimensional shape, flow fields on which 5 streamwise-horizontal (x−y) plane at inverval of 30mm (0.18s) (figure 9(b)) were measured, and the third plane (P3) coincides with the center plane (figure 2(b)). The surface of model is painted black to reduce reflection of laser light. Table 2 shows details of each plane, including field-of-view (FoV) and spatial resolution. The interrogation window was size of 16×16 pixels which is recursively refined from 32×32 pixels based on the iterative application of cross correlation analysis. The interrogation windows were overlapped by 50%, and spatial resolution of each measurements are shown is table 2. 4008 vector fields are averaged to obtain a fully converged velocity field. Assessing u_{rms} value at the point on which u_{rms} reaches maximum, the value is converged when the number of instantaneous fields is larger than 4000. Time intervals of each measurement is small enough to satisfy one-quarter rule. Every flow fields are nondimensionalized using freestream velocity (U) and chordlength (c).

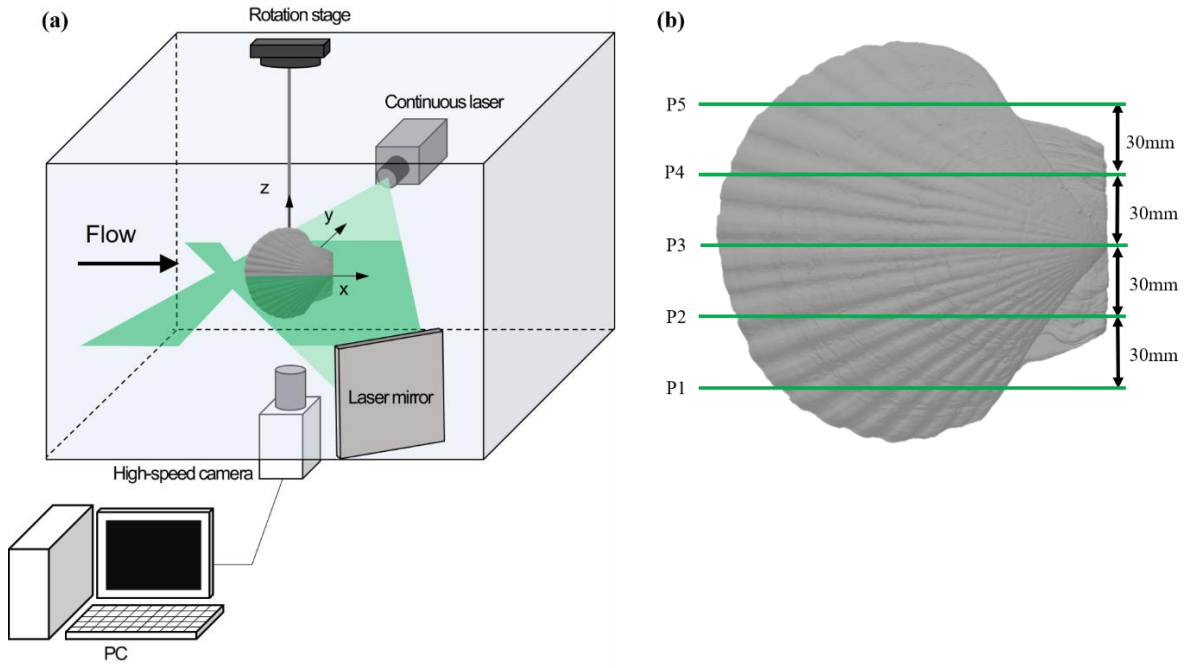

Figure 9. (a) Schematic diagram of the experimental setup for PIV measurement and (b) planes in which flow field is measured by PIV

Plane	FoV (mm)	Spatial resolution	Reynolds number
P1	215 × 134.4	0.0081c (1.34mm)	45000
P2	225.3 × 140.8	0.0085c (1.41mm)	45000
P3	235.5 × 147.2	0.0089c (1.47mm)	20000, 30000, 45000
P4	245.8 × 153.6	0.0093c (1.54mm)	45000
P5	258.6 × 161.6	0.0098c (1.62mm)	45000

Table 2. Details of each flow fields.

3. Results and discussion

3.1. Kinematics of swimming scallop

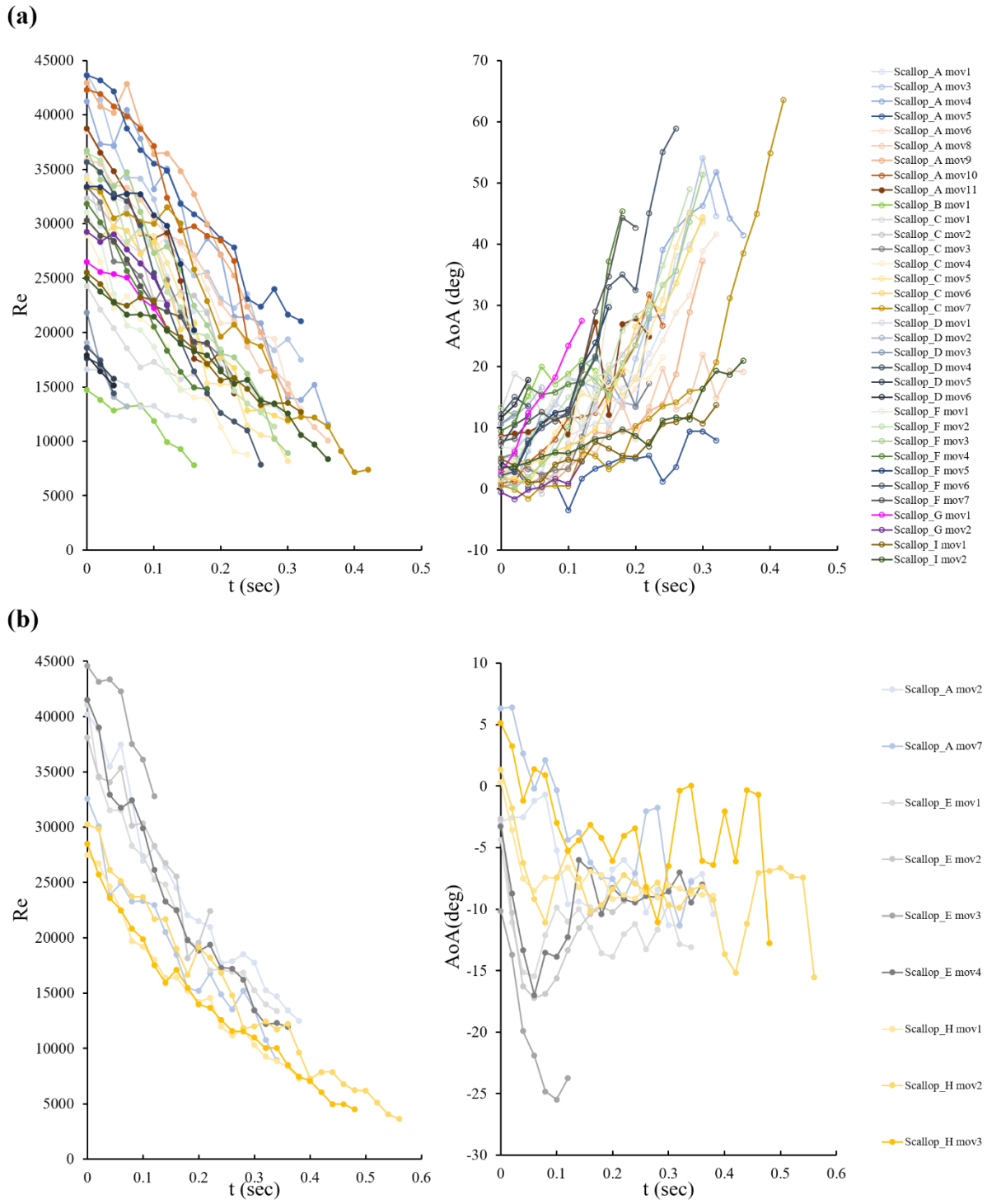

Figure 10. Variations of Reynolds number and angle of attack with swimming time for all movements; (a) positive pitching motions and (b) negative pitching motions.

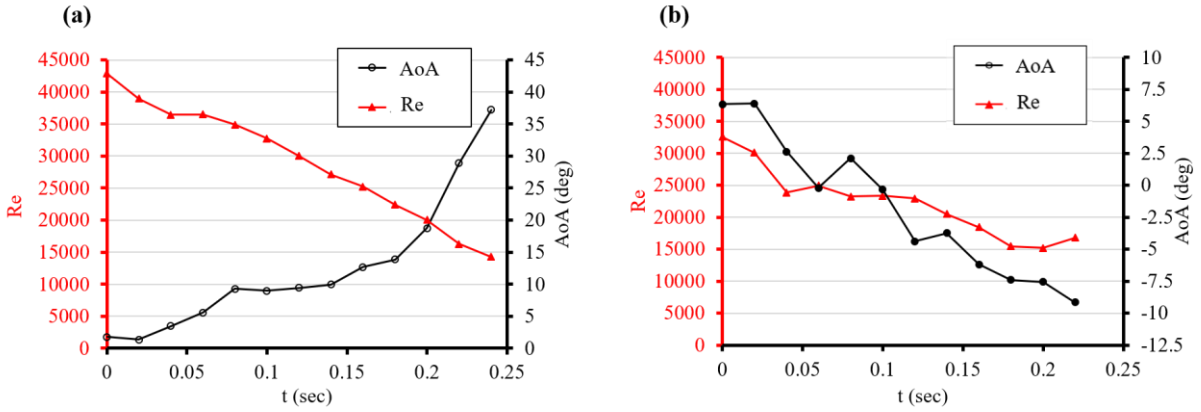

Figure 11. Variations of the Reynolds number and angle of attack with swimming time for 2 representative movements; (a) positive pitching motion and (b) negative pitching motion.

Figure 10 shows measured kinematic data of all movements and figure 11 shows data of representative 2 movements. Kinematic data consists of the variations in Reynolds number and AoA with swimming time. Image was analyzed from when the scallop's two valves were completely closed so no thrust was generated to when the scallop was no longer advancing. The Reynolds number graph is not finally zeroed because the scallops standing by the increased or decreased pitch angle have their velocity to lie on the ground again. Figure 10(a) and 11(a) show positive pitching motion and Figure 10(b) and 11(b) show negative pitching motion. Positive pitching motion is the motion during that the scallop advances with increasing pitch angle, and negative pitching the motion is motion during that the scallop advances with decreasing pitch angle. As shown in figure 10(a), in the case of positive pitching motion, AoA keeps increasing since the start of swimming, and the Reynolds number based on the instantaneous velocity keeps decreasing. AoA increases from 0° to 70°, and Reynolds number decreases from 45,000. Although AoA is increased as 70°, forces and moment are measured in the range of 0°-50°, because over the AoA of 50°, the velocity is very low. The scallop is attached to the ground, so the flow around the scallop is in ground effect. In the case of negative pitching motion, The Reynolds number is decreased from 45000, similar with positive pitching motion. However, AoA is decreased to negative value, different with positive pitching motion.

In figure 12, when the scallop advances to left, the trajectories of the scallop are shown at intervals of 0.1 seconds. Among 41 movements of all samples, positive pitching motions are 32 and the remaining 9 are negative pitching motions. Positive pitching motion was more common than negative pitching motion. Despite being a zigzag swimmer, the range of angle of attack is similar with level swimmer (Morton, 1980).

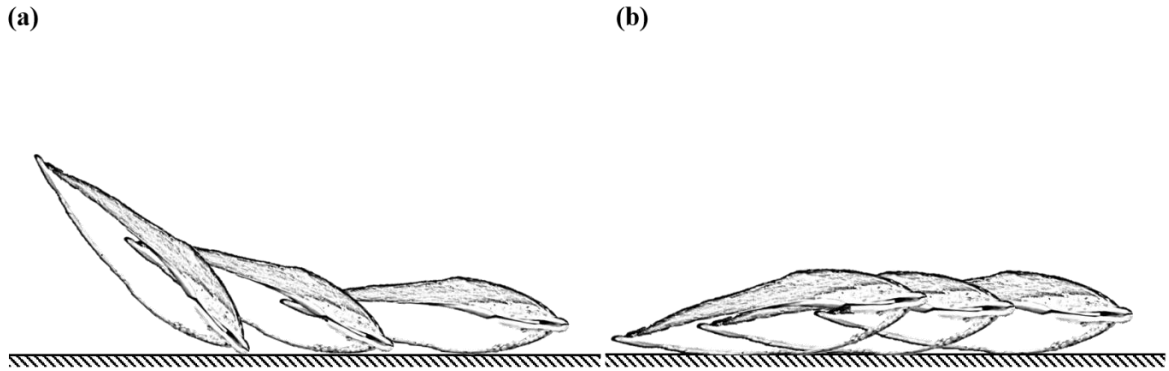

Figure 12. Trajectories of scallop in 0.1 second time intervals; (a) positive pitching motion and (b) negative pitching motion.

3.2. Forces and moment measurement in ground effect

The hydrodynamic forces and moment which the scallop is applied in ground effect was measured by water tunnel experiment, and the results are shown in the figure 13. When the angle of attack is lower than the stall angle, lift is not changed as Re, and after stall, the lift is increased slightly as Re increases. From AoA=22°, the stall occurred, lift slope is concave down and drag is increased more steeply than before. At AoA is about 35°, the lift reaches maximum value.

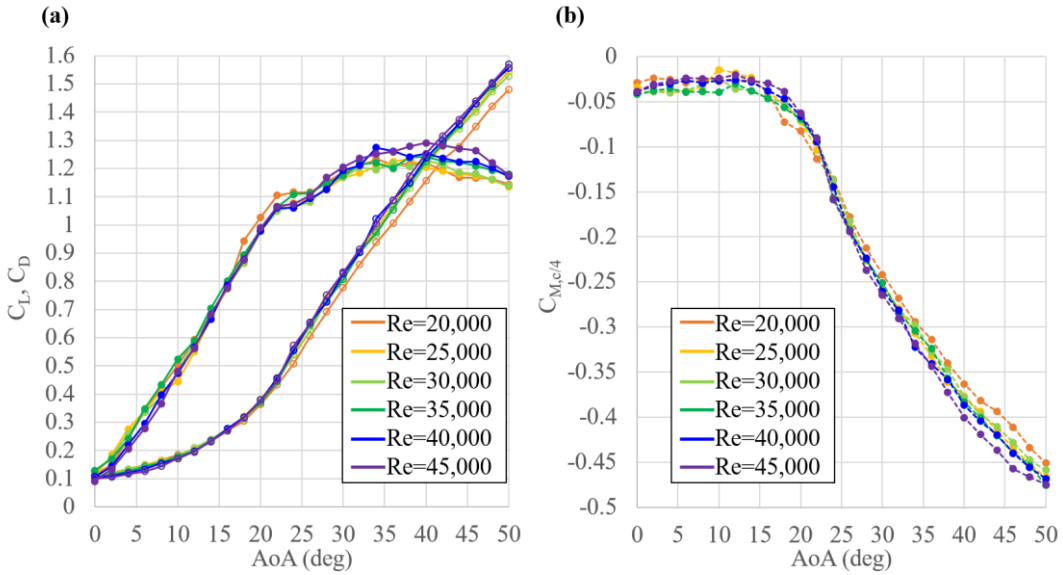

Figure 13. Forces and moment measurement in ground effect; (a) force; C_L (Closed circle) C_D (Open circle) and (b) moment; $C_{M,c/4}$.

Thomas and Taylor (2001) suggested that the nose-down pitching moment for gliding animals, which means negative pitching moment ($-C_{M,c/4}$). The nose-down pitching moment should be

increased as increasing AoA to acquire longitudinal static stability. The more steeply $-C_{M,c/4}$ is increased, the more stable the flight is. $C_{M,c/4}$ of the model is decreased as shown in figure 13(b), so the scallop swimming is stable.

3.3. Swimming trajectory simulation

Based on the measured forces and moment, the trajectory was computed as shown in figure 14(a). In figure 14(a), circle means leading edge of the scallop, and the scallop procced to right. The recorded trajectory of the actual scallop and the computed trajectory tend to be similar, and the velocity, AoA, and pitch angle change similarly, as can be seen in the figure 14(b). Therefore, quasi-steady state can be assumed in scallop swimming, and hydrodynamic forces and moment measured by water tunnel experiment can be regarded as the force applied on swimming actual scallop. There is difference at pitch angle and velocity because the scallop was assumed to be a zero-volume rod.

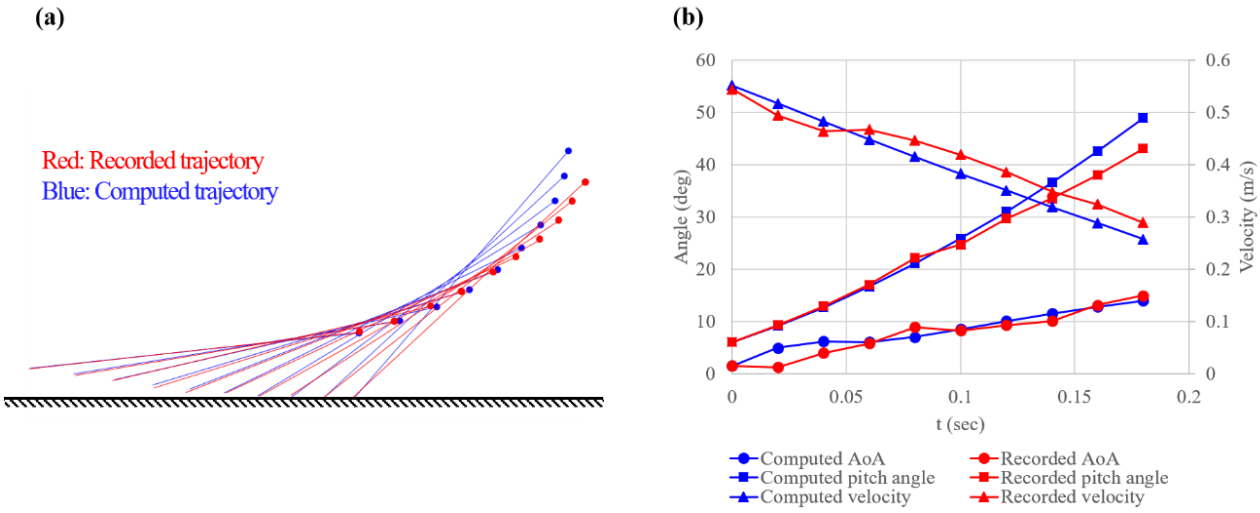

Figure 14. Trajectory computation results in 0.05 second time intervals; (a) computed trajectory compared with recorded trajectory of actual scallop, and (b) quantitative comparison with each trajectory.

3.4. Forces and moment measurement out of ground effect

Figure 15 shows the results of measured forces and moment out of ground effect. Since camber is 0, the lift and moment are almost zero when the angle of attack is 0 degrees. When the angle of attack is lower than stall angle, the Reynolds number effect appears. When the Reynolds number is low, the lift

coefficient is concave up as increasing angle of attack, but as the Reynolds number increases, the lift coefficient curve gradually becomes more linear. The stall occurs twice, unlike when forces and moment are measured in the ground effect. The lift slightly decreases after the first stall, then increases again, and the lift decreases significantly after the second stall. The moment coefficient in the quarter chord ($C_{M,c/4}$) is almost zero at $AoA = 0°$. After slight increasing, the moment is decreased until the second stall.

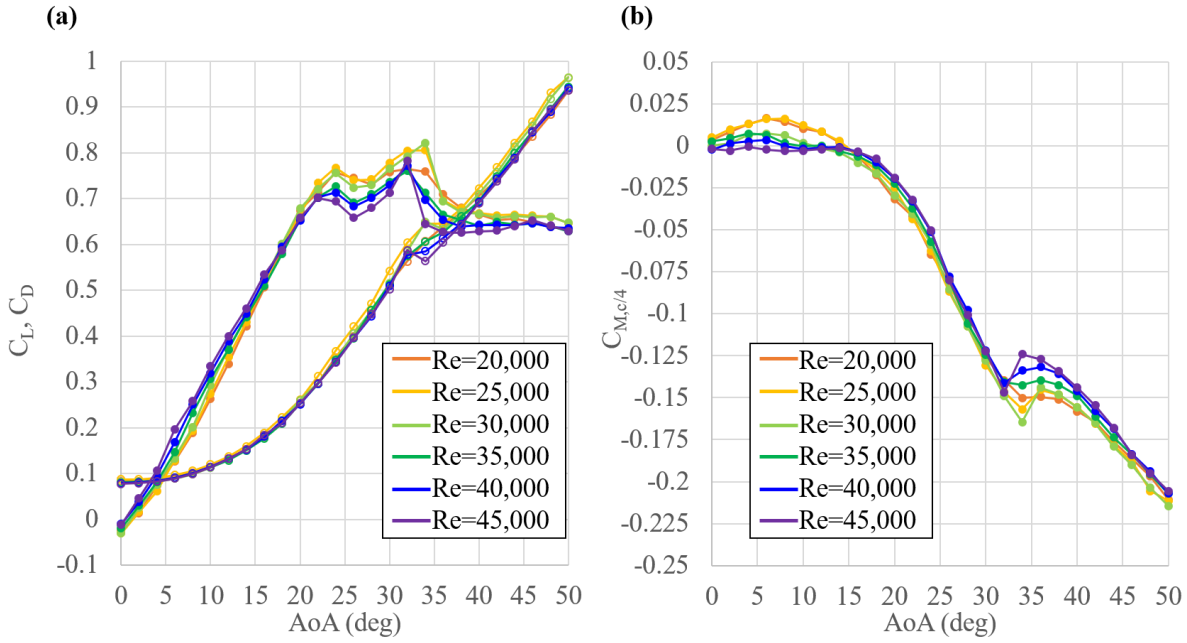

Figure 15. Force and moment measurement out of ground effect; (a) force; C_L (Closed circle), C_D (Open circle) and (b) moment; $C_{M,c/4}$.

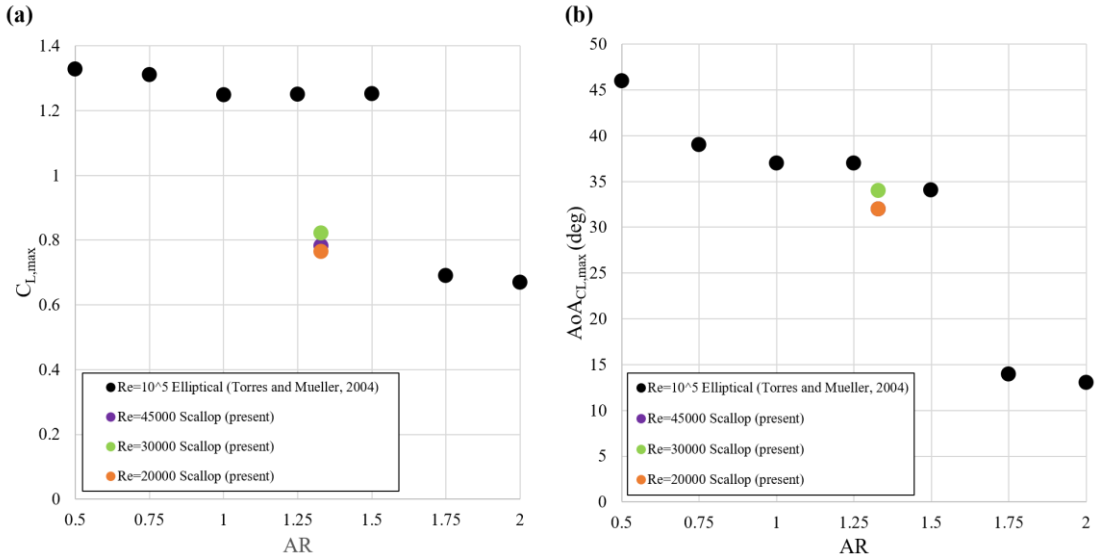

Figure 16. Variations of (a) $C_{L,max}$ and (b) $AoA_{CL,max}$ of the scallop and elliptical planform wing as aspect ratio (AR).

Figure 16(a) shows the maximum value of C_L ($C_{L,max}$) which is the value right before stall, and figure 16(b) shows the value of angle of attack, when C_L has the maximum value ($AoA_{CL,max}$) which is stall angle. According to Torres and Mueller (2004), there is transition zone for $C_{L,max}$ and $AoA_{CL,max}$ in the aspect ratio range between 1.5 and 1.75 (figure 16(a) and (b)). When aspect ratio is lower than the transition zone, wing-tip vortices can energize the flow on the upper side of the model, so separation is delayed to high AoA. However, as aspect ratio increases, the wing-tip vortex is weakened, thus the separation no longer delayed.

Scallop planform is similar with ellipse, so $AoA_{CL,max}$ of the model matches the value of elliptical planform wing (Torres and Mueller 2004), but $C_{L,max}$ of the scallop is less than the value of reference. This is because the model is already stalled once.

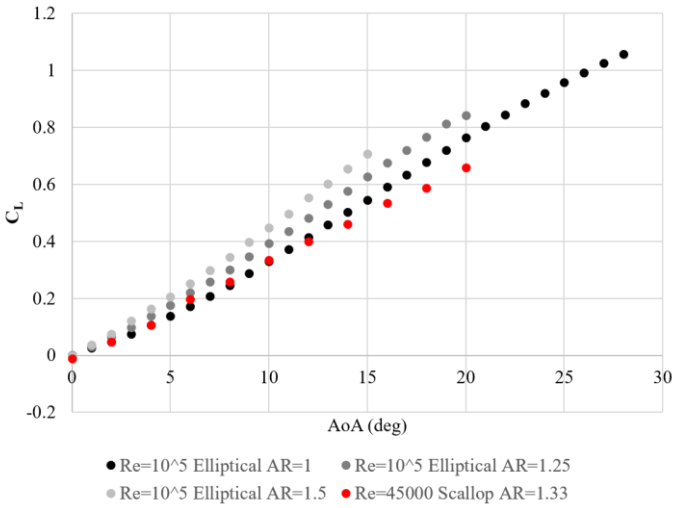

Figure 17. Variations of lift slope as aspect ratio (AR).

As shown in figure 17, lift slope of elliptical wing measured by Torres and Mueller (2004) is decreased when AR is decreased, so high AR wing has better hydrodynamic performances than low AR wing before stall. However, the stall of low AR wing occurs at larger angle of attack than high AR wing as shown in figure 16. Thus, the maximum lift coefficient is increased as decreasing AR. The scallop is thick, so wake region is formed behind the scallop. The wake region makes lift slope of the scallop smaller than elliptical wing.

Figure 18 shows the position of the center of pressure (h_{CL}) with the change of the angle of attack and measured h_{CL} is compared with the result of Torres and Mueller (2004). h_{CL} is defined as

$$\mathbf{h_{CL}} = \frac{x_{CL}}{c} \tag{62}$$

where x_{CL} is the distance between center of pressure and the leading edge of the model. h_{CL} is calculated by following equation.

$$\mathbf{h_{CL}} = \mathbf{0.25} - \frac{C_{M,c/4}}{C_L cos\alpha + C_D \sin\alpha} \tag{63}$$

When the angle of attack is low, the effects of linear lift, which can be obtained with the Kutta-

Joukowski theorem, closely match the center of pressure with the 1/4 chord, the aerodynamic center. However, if the angle of attack of the scallop increases larger than 15 degrees, the position of the center of pressure will move downstream. This indicates that the effect of nonlinear lifts induced by the tip vortex due to the low aspect ratio is increasing. Compared to the results of Torres and Mueller (2004), the model results agree well with the elliptical flat wing of which aspect ratio is 1.25.

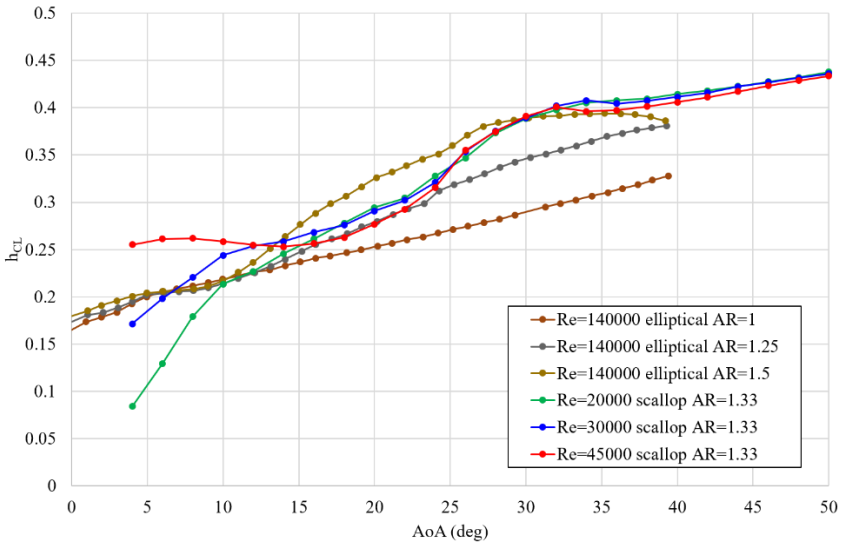

Figure 18. Changes of center of pressure position (h_{CL}) as angle of attack

3.5. Comparison with measurements in ground effect and out of ground effect

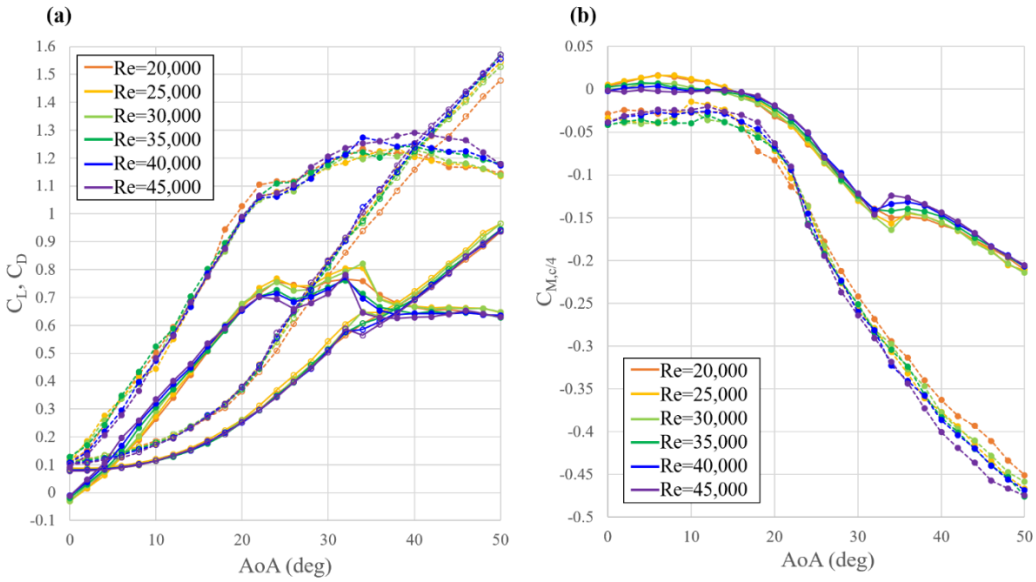

Figure 19. Comparison with measurements in ground effect (dashed line) and out of ground effect (solid line); (a) C_L (closed circle), C_D (open circle) and (b) $C_{M,c/4}$.

For a 2-dimensional body, such as airfoil, drag is decreased, and lift is increased in ground effect. In ground effect, Karman vortex shedding is prevented, so drag of airfoil is decreased, and pressure at the lower surface is increased, so lift of airfoil is increased (Kim and Geropp 1988; Choi and Lee 2000; Ahmed and Sharma 2006). In the other hand, for a 3-dimensional body, such as finite wing, tip vortex is weakened by ground, so lift is increased, and drag is decreased in ground effect (Wieselsberger 1922; Phillips and Hunsaker 2013; Traub 2015).

As shown in figure 19, lift and drag is increase and moment is decreased for every angle of attack in ground effect. It is expected that 3-dimensional convex bottom of the model strengthens tip vortex in ground effect. This is because the closer to the tip from the root, the greater the distance between ground and the model.

The quarter-chord moment is decreased, and the slope also became steeper in ground effect. That is nose-down moment is increased more steeply Therefore the scallop can swim more stable near the ground.

3.6. Flow-field visualization

Figure 20 is representative flow field measured by PIV when the angle of attack is 0° on center plane. In the figure 20, the gray region is the cross section of the model for each plane, and the black region is not clearly measured region because of too much light reflection. Wake region is formed at the rear (downstream) of the model due to high adverse pressure gradient caused by the thickness of 0.28c and blunt trailing edge. Karman vortex shedding is shown in figure 20(d). Wake region is also formed on the other planes (P4, P5). It was also shown by Lind *et al*. (2014).

Figure 21 shows flow field on center plane, P3, as Reynolds number of 20,000, 30,000 and 45,000. Shown in figure 21, separation is delayed downstream as Re increased, thereby lift is increased at low AoA. To analyze separation delay quantitatively, the chordwise distances between leading edge and separation point (x_{sep}) are found according to the Reynolds number when the angle of attack is 6° and 12° (table 3). At $\mathrm{AoA} = 6°$, separation points when Re=20000 and 30000 are the same, but when Re=45000, separation is delayed. At $\mathrm{AoA} = 12°$, separation is also delayed when $\mathrm{Re} = 30000$. This result is consistent with the force measurement results. This is because the flow with high Reynolds number has more momentum to overcome the adverse pressure gradient.

Figure 22 and 23 show the change of the flow field with the angle of attack on 3 planes when the angle of attack is around the first stall angle, and Re=45,000. In planes near the tip (P1 and P5), the flow is totally separated from the scallop surface at AoA = 22° in contrast to center plane (P3) on

which flow field is not totally separated. This is because the local Reynolds number near the tip based on the chordlength of the section is lower than the center plane (P3). At AoA = 24°, the separation bubble from the leading edge meets the wake region behind (downstream) the model on every plane and does not reattach to the surface, resulting in the first stall. When the AoA is greater than 26°, tip vortices help the flow attach to the upper surface of the model and the lift increases again.

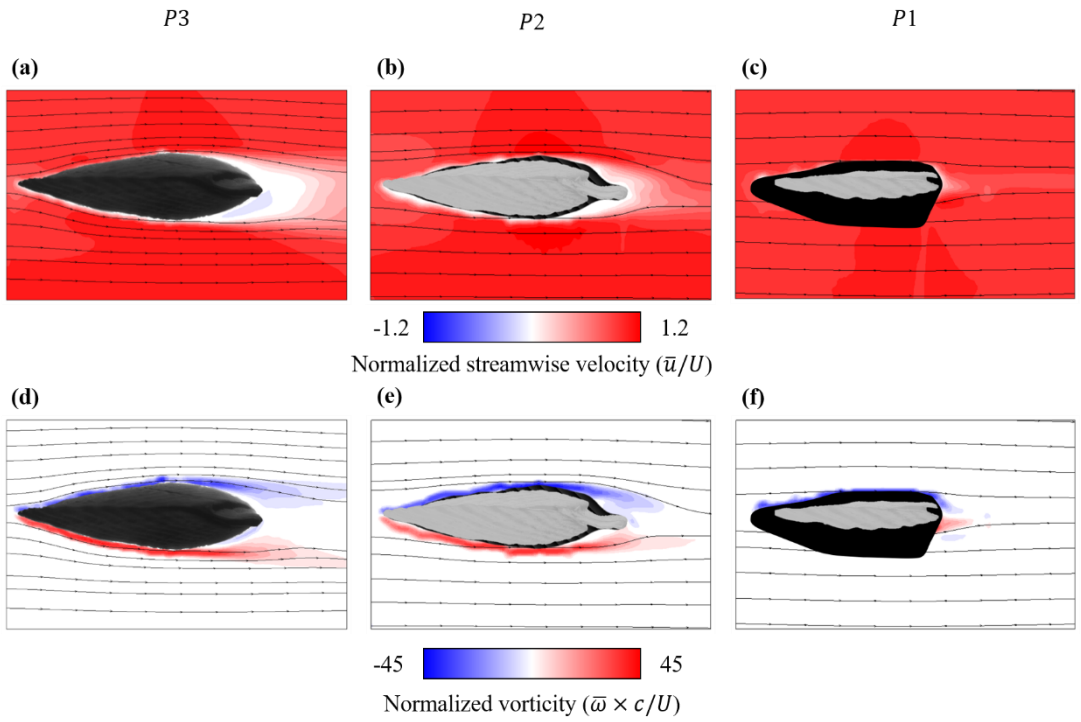

Figure 20. Time-averaged u and vorticity (ω) contours and streamlines when AoA=0°, and Re=45,000 on planes of P1, P2, and P3.

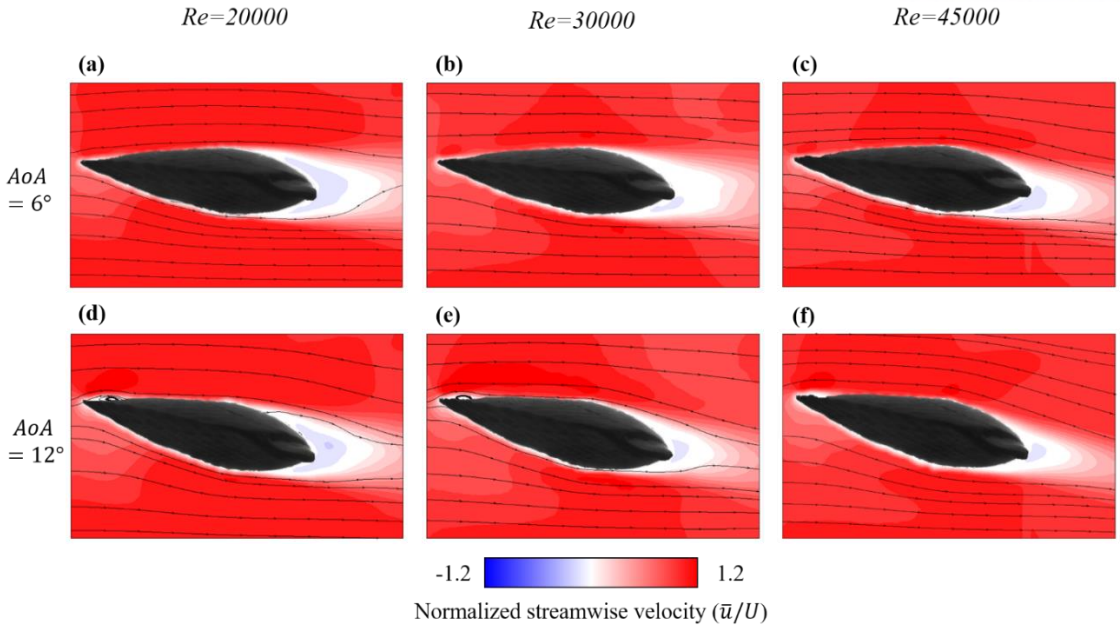

Figure 21. Time-averaged u contours and streamlines when AoA=6° and 12°, and Re=45,000 on plane of P3.

Re	AoA = 6°	AoA = 12°
20000	0.73c.	0.73c
30000	0.73c	0.77c
45000	0.89c	0.89c

Table 3. Locations of separation point (x_{sep}) as Re at AoA=6° and 12°.

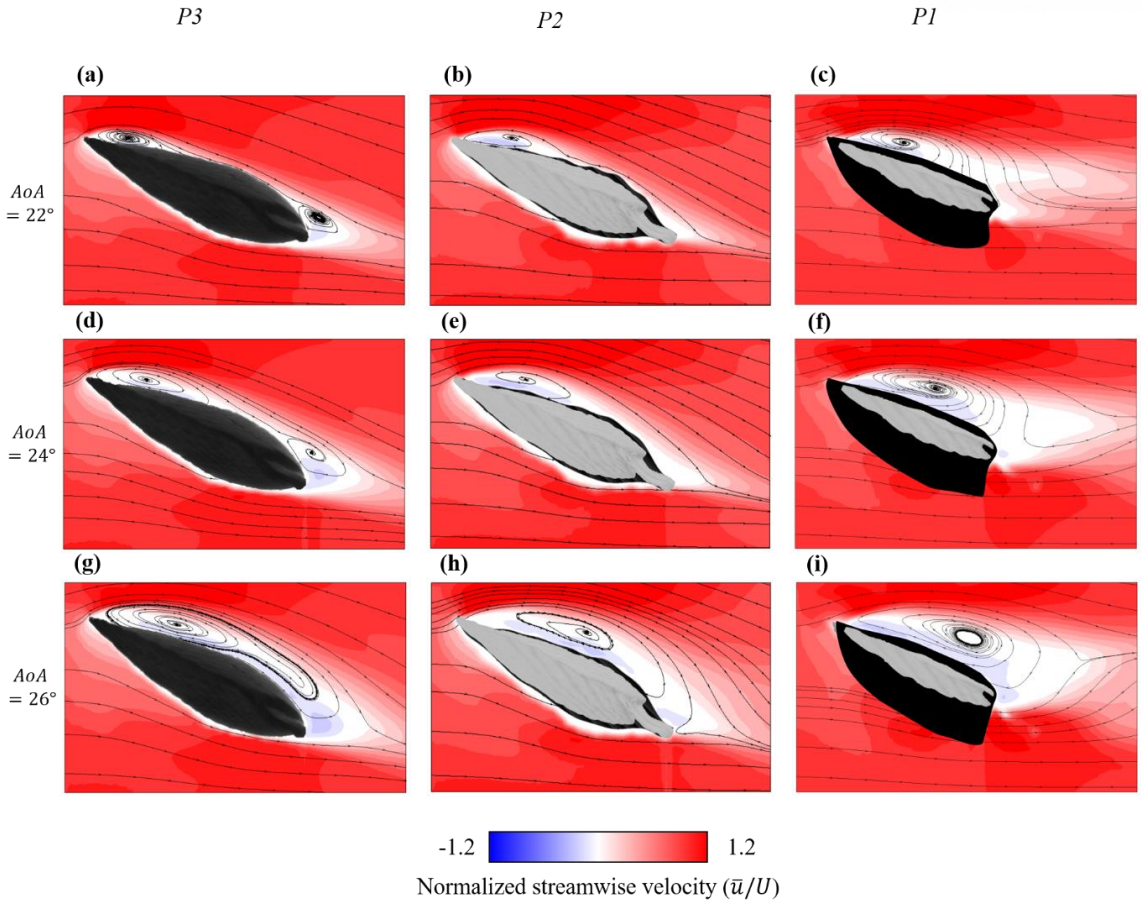

Figure 22. Time-averaged u contours and streamlines when AoA=22°, 24° and 26°, and Re=45,000 on planes of P3, P2 and P1.

Looking at the v contours of the P3 plane and the P2 plane (figure 23(g) and (h)), downwash was formed on the suction side of the model, caused by tip vortex, so it is called tip-vortex induced downwash. There is upwash behind the section of the model on plane P1 (figure 23(f) and (i)). On the other hand, there is downwash at the same point on contour on plane P2 (figure 23(e) and (h)). This is because the tip vortex is formed along the tip of the model and passes between plane P2 and P1, so upwash is shown in P1, and downwash is shown in P2.

In figure 24, vorticity grows from the leading edge and this is called leading edge vortex (LEV). The LEV proceeds to negative y direction on P3 and P2 planes (figure 24(g) and (h)) although stall already occurs, because LEV affected by tip-vortex induced downwash. Hence, flow is reattached to the surface of the model, and lift is increased although stall already occurs.

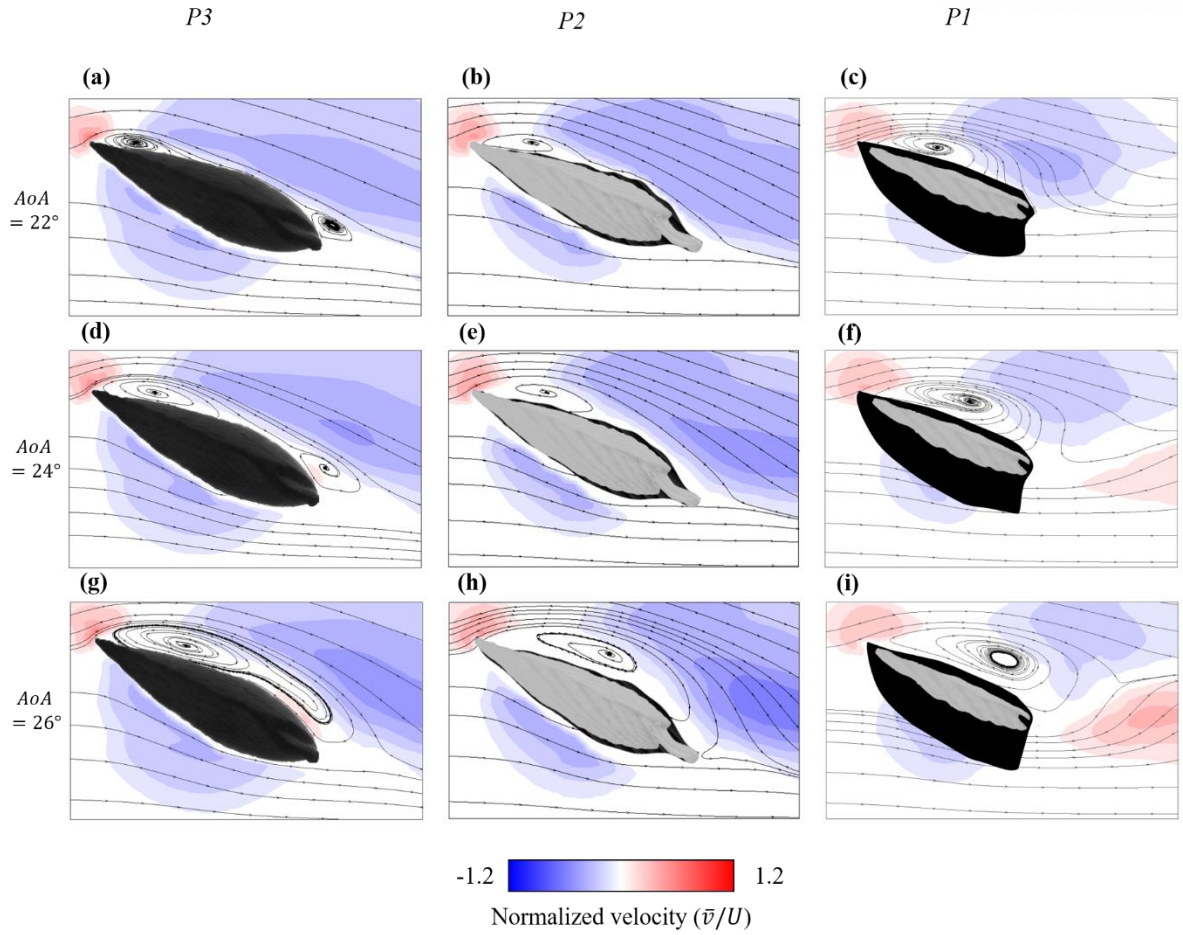

Figure 23. Time-averaged v contours and streamlines when AoA=22°, 24° and 26°, and Re=45,000 on planes of P3, P2 and P1.

When the angle of attack becomes 36°, in figure 25(a), tip-vortex induced downwash are not formed over the model as increasing AoA, so the vorticity contour (figure 25(b)) shows that the gap between the model and the LEV is considerably wider. This wide gap indicates LEV is no longer interact with tip-vortex induced downwash on the model. Therefore, tip vortices no longer help flow attach to the surface and the flow is separated, resulting in a significant reduction in lift and the second stall.

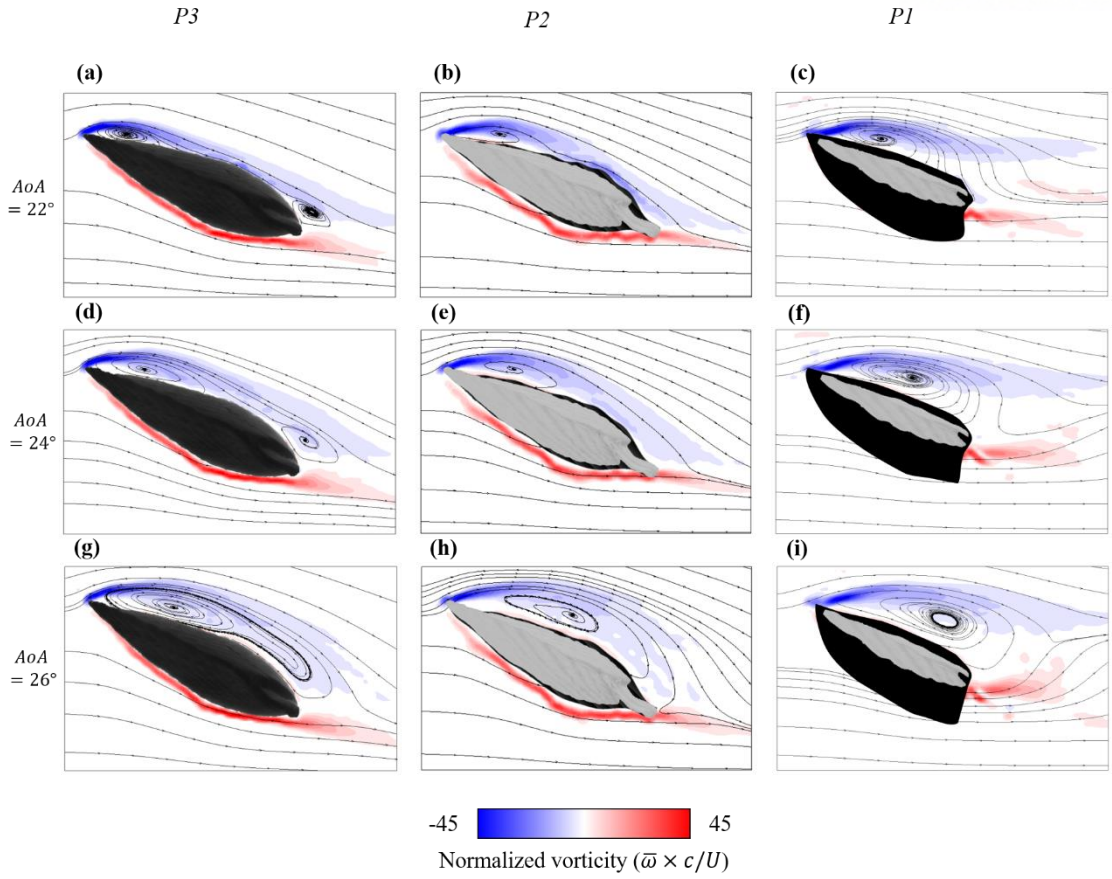

Figure 24. Time-averaged vorticity contours and streamlines when AoA=22°, 24° and 26°, and Re=45,000 on planes of P3, P2 and P1.

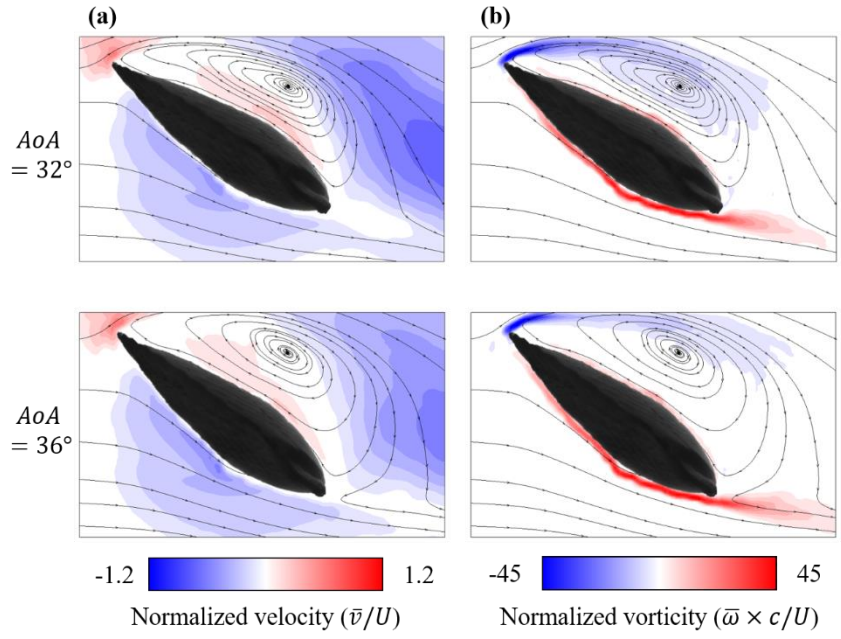

Figure 25. Time-averaged (a) v-component and (b) vorticity contours and streamlines when AoA=32°, and 36°, and Re=45,000 on planes of P3.

4. Conclusions

To know hydrodynamic characteristics of the scallop, swimming motions of the actual scallop are recorded by 2 high-speed cameras, and analyzed to obtain kinematic data of the scallop, such as Reynolds number and angle of attack. The scallops were attached to the ground when swimming, and generally moved with increasing pitch angle. While the scallop swims in a positive pitching motion, angle of attack is increased to 70°, Reynolds number is decreased from 45000.

Based on the obtained kinematic data, hydrodynamic forces and moment in ground effect are measured by water tunnel experiment. Trajectory is computed with the results of forces and moment measurement and compared with recorded trajectory of actual scallop swimming to verify quasi-steady assumption of scallop swimming motion, and hydrodynamic similarity between the flow around actual scallop swimming, and the flow around scallop model in water tunnel experiment.

After verifying hydrodynamic similarity between actual scallop and model, hydrodynamic characteristics of the scallop out of ground effect is measured by direct force measurement, and particle image velocimetry.

Comparing the forces and moment with those in ground effect, both lift and drag are decreased in all region of Re and AoA. The reason of this phenomenon is not known, but it is expected that the shape of scallop bottom, which is convex in spanwise axis, contributes to increasing lift and drag. Counterintuitively, tip vortices seemed to be strengthened because of convex bottom of the model, so further research about ground effect on the scallop is needed.

Since the scallop, *Patinopecten yessoensis*, is thick and has blunt trailing edge, a wake region is formed in the vicinity of the trailing edge despite of low AoA, 0°. The size of the wake region before the stall becomes narrower as the Reynolds number increases, and thus the lift coefficient before the stall increases as the Reynolds number increases.

A separation bubble is formed from the sharp leading edge of the scallop. When the angle of attack is 24°, the first stall occurs when the reattachment point of separation bubble encounters the wake near the trailing edge. Then the flow is no longer reattached to the surface of the scallop. Immediately after the first stall (AoA=26°), tip-vortex induced downwash reattaches LEV to the surface of the scallop and increases the lift again.

When the angle of attack is increased to 34°, tip-vortex induced downwash is not formed over the model and no longer make leading edge vortex attach to the surface, resulting in a second stall. Further study on the tip vortex structure as the angle of attack is needed.

Reference

1. Ahmed, M. R. and Sharma, S. D. 2006 An investigation on the aerodynamics of a symmetrical airfoil in ground effect. *Exp. Therm. Fluid. Sci.* **29**, 633-647.

2. Anderson, E. J., MacGillivray, P. S. and DeMont, M. E. 1997 Scallop shells exhibit optimization of riblet dimensions for drag reduction *Biol. Bull.* **192**, 341-344.

3. Bayne, B. L. and Newell R. C. 1983 Physiological energetics of marine molluscs *The Mollusca* vol 4 ed A S M Saleuddin and K M Wilbur (New York: Academic Press), pp 407–515.

4. Caddy, J. F. 1968 Underwater observations on scallop (*Placopecten magellanicus*) behaviour and drag efficiency *J. Fish. Board Can.* **25**, 2123-2141.

5. Chapman, C. J., Main, J., Howell, T., and Sangster, G. I. 1979 The swimming speed and endurance of the queen scallop *Chlamys opercularis* in relation to trawling *Prog. Underwat. Sci. **4***, 57-72.

6. Choi, H., Park, H., Sagong, W. and Lee, S. I. 2012 Biomimetic flow control based on morphological features of living creatures *Phys. Fluids* **24**, 121302.

7. Choi, J. H. and Lee, S. J. 2000 Ground effect of flow around an elliptic cylinder in a turbulent boundary layer. *J. Fluid Struct.* **14**, 697-709.

8. Dadswell, M. J., and Weihs, D. 1990 Size-related hydrodynamic characteristics of the giant scallop, *Placopecten magellanicus* (Bivalvia: Pectinidae). *Can. J. Zool.* **68**, 778-785.

9. Dautov, S. S. h. and Karpenko, A. 1984 Behavior and mechanisms of locomotion of two species of scallops from the Sea of Japan. *Sov. J. Mar. Biol.* **9**, 271-275.

10. Feder, H. M. 1955 On the methods used by the starfish Pisaster ochraceus in opening three types of bivalve molluscs *Ecology* **36**, 764-767.

11. Gosling, E. 2008 *Bivalve molluscs: biology, ecology and culture*. John Wiley & Sons.

12. Gruffydd, L. D. 1976 Swimming in *Chlamys islandica* in relation to current speed and an investigation of hydrodynamic lift in this and other scallops *Norw. J. Zool.* **24** 365-378.

13. Hayami, I. 1991 Living and fossil scallop shells as airfoils: an experimental study *Paleobiology* **17**, 1-18.

14. Kim, M. S. and Geropp, D. 1998 Experimental investigation of the ground effect on the flow around some two-dimensional bluff bodies with moving-belt technique. *J. WIND ENG. IND. AEROD.* **74**, 511-519.

15. Lind, A. H., Lefebvre, J. N. and Jones, A. R. 2014 Time-averaged aerodynamics of sharp and blunt trailing-edge static airfoils in reverse flow. *AIAA J.* **52**, 2751-2764.

16. Martin, R. E., Carter, E. P., Davis, L. M. and Flick Jr, G. J. 2000 *Marine and freshwater products handbook*. CRC Press.

17. Millward, A. and Whyte, M. A. 1992 The hydrodynamic characteristics of six scallops of the Super Family Pectinacea, Class Bivalvia *J. Zool. Lond.* **227**, 547-566.

18. Moore, J. D. and Trueman, E. R. 1971 Swimming of the scallop, *Chlamys opercularis* (L.) *J. Exp. Mar. Biol. Ecol.* **6**, 179-185.

19. Morton, B. 1980 Swimming in *Amusium pleuronectes* (Bivalvia: Pectinidae) *J. Zool.* **190**, 375-404

20. Phillips, W. F. and Hunsaker, D. F. 2013 Lifting-line predictions for induced drag and lift in ground effect. In *31st AIAA Applied Aerodynamics Conference* (p. 2917).

21. Sagong, W., Kim, C., Choi, S., Jeon, W. P. and Choi, H. 2008 Does the sailfish skin reduce the skin friction like the shark skin? *Phys. Fluids* **20**, 101510

22. Silina, A. V. 2008 Long-term changes in intra-and inter-specific relationships in a community of scallops and sea stars under bottom scallop mariculture. *J. Shellfish Res.* **27**, 1189-1195.

23. Stanley, S. M. 1970 *Relation of shell form to life habits of the Bivalvia (Mollusca)* (Vol. 125). Geological Society of America.

24. Thomas, A. L. and Taylor, G. K. 2001 Animal flight dynamics I. Stability in gliding flight. *J. Theor. Biol.* **212**, 399-424.

25. Torres, G. E. and Mueller, T. J. 2004 Low aspect ratio aerodynamics at low Reynolds numbers. *AIAA J.* **42**, 865-873.

26. Traub, L. W. 2014 Experimental and analytic investigation of ground effect. *J. Aircraft* **52**, 235-243.

27. Vogel, S. 1997 Squirt smugly, scallop! Nature **385**, 21-22.

28. Wieselsberger, C. 1922 Wing Resistance Near the Ground. Technical Report NACA-TM-77, NACA.